

**Little Book
of
Dynamic Buckling**

Herbert E. Lindberg

**September 2003
LCE Science/Software**

Preface

A graduate program in mechanics (often part of aero/astronautical, civil or mechanical engineering) generally includes a short series on elastic stability of structures. Within the confines of available time, focus is on stability under static loading, with dynamic loading from earthquakes, aerodynamics, impact and so on touched on only briefly except for students with thesis topics in these areas. This short book is intended as a brief introduction to dynamic buckling that can be covered in the limited time available in a broad graduate program. It is small and inexpensive enough that the student can own his or her own copy, rather than simply taking notes during lectures extracted by the teacher from the several full-size texts available on this topic, including one by the present author.

The book introduces concepts of dynamic buckling in the simplest possible context for each phenomenon. The phenomena treated all fall under the definition of *dynamic stability of structures under time-varying parametric loading*. The goal is met by treating simple bars under axial loads, rings under lateral pulse loads, and cylindrical shells under radial and axial loads. The present document includes only a general introduction and then comprehensive presentation of theory and experimental data for bars under static and impact loads. Sections on rings and shells will be made available as orders are received.

In all cases motion is precipitated by inevitable imperfections in structural shape. Sometimes these appear as a simple parameter, as in the eccentricity of impact. In most cases, however, the imperfections are unknown functions of surface coordinates. In later chapters, two methods are introduced to describe shape imperfections: random coefficients of modal shapes (probabilistic analysis) and worst-case imperfection shapes found by convex modeling (uncertain shapes described by convex sets). Both types of imperfections are used and compared in closed-form solutions for these structures, and also form the basis for introducing initial shapes into finite element calculations of more general structures the student is likely to encounter in engineering practice.

This little book is distributed freely as a group of pdf files posted on the Internet at

www.lindberglce.com/tech/buklbook.htm

These files can be displayed and printed by Adobe Acrobat, available as a free download from the Adobe Web site if you don't already have it. A small computer code is also available at the above Web address. It creates and displays movies of a bar buckling from axial impact, with parameters specified by the user.

Although no special permission is needed to download these files, if you find the book useful as part of a course you are teaching or taking, or as a tool in your professional work, the author asks that you contribute a development and distribution fee of \$10. Please write a check for that amount to Herbert E. Lindberg and mail it to

LCE Science/Software
18388 Chaparral Drive
Penn Valley, CA 95946-9234

Chapter 1

Forms of Dynamic Stability

The phenomena treated in this little book all fall under the definition of *dynamic stability of structures under time-varying parametric loading*. That is, the driving term appears as a parameter that multiplies the structural displacement coordinate, rather than as a forcing function on the right hand side of the equation of motion as in forced structural vibrations. For example, in the simple bar treated in the next chapter the equation of motion for lateral displacement $y(x, t)$ from initial shape $y_0(x)$ is

$$EI \frac{\partial^4 y}{\partial x^4} + P(t) \frac{\partial^2}{\partial x^2} (y + y_0) + \rho A \frac{\partial^2 y}{\partial t^2} = 0$$

in which EI is bending stiffness, ρA is lineal density, and x and t are axial coordinate and time, respectively. Note that the axial load P multiplies displacement y on the left hand side of the equation; that is, it is a parameter (coefficient) of the equation. Following conventional equation display, a lateral load $p(x, t)$ that produces simple forced vibrations would appear as a driving function on the right hand side of the equation.

Figure 1.1 illustrates two forms of dynamic buckling in a bar under axial load, both resulting from the above equation of motion. In the bar on the left the load oscillates at a frequency twice the lowest bending frequency ω_1 of the unloaded bar. The amplitude of motion increases because each time the bar bends to one side or the other the axial load $P \sin 2\omega_1 t$ approaches its maximum and induces additional bending.

The bending shape and oscillations are very similar to what would occur under a lateral load $p \sin \omega_1 t \sin \pi x / L$ that excites this mode of vibration. The unbounded growth that results from this forcing function (in the absence of damping or nonlinear effects) is resonant forced vibration, a central topic of conventional structural dynamics. In the case of axial load $P \sin 2\omega_1 t$ the motion is resonant dynamic buckling. Because of the similarity to resonant vibrations, this type of dynamic buckling can be called *vibration buckling*.

In the bar on the right in Figure 1.1 the load is applied as a single pulse of amplitude very much larger than the static buckling load of the bar. This occurs, for example, in a bar that impacts at velocity v against a massive rigid object. The impact stress $\rho c v$ (c is axial-stress wave velocity) can be larger than the “static” buckling stress of high-order bending modes with very short wavelengths, even at modest impact velocities. The resulting buckled form consists of many waves along the length of the bar, and

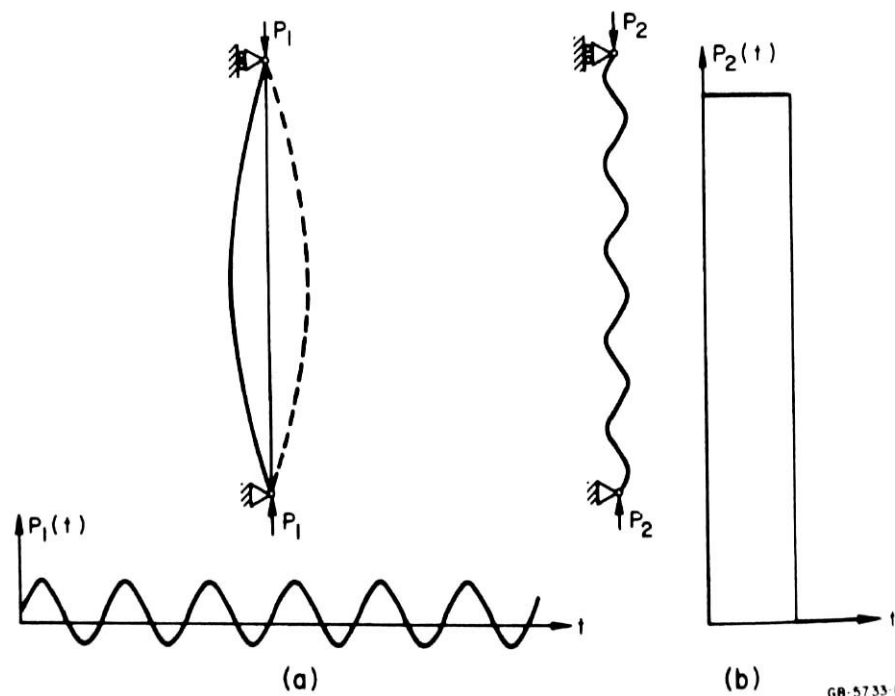


Figure 1.1: Vibration buckling (left) and pulse buckling (right).

while the load is applied the buckling increases monotonically rather than oscillating as in the bar on the left. The buckle shape is idealized to a single mode in the sketch, and other complexities such as axial wave propagation enter into the actual problem, but the fundamentals of the load and idealized buckle shape are correct. Because such buckling is induced by single load pulses of large amplitude, this type of dynamic buckling can be called *pulse buckling*.

Figure 1.2 is a series of ultra-high speed framing camera photographs of an aluminum strip following impact against a massive jaw at the bottom of the photos. The impact condition was produced by pulling the strip, which was many times longer than the few inches seen in the photos, in a tensile machine and then suddenly cutting it near its upper end with a small explosive charge. The resulting compressive relief wave traveled down to the jaw where it reflected, again as a compressive wave, and produced an axial compression equal to the initial tension.

Buckling is concentrated near the impacted end because the axial load is experienced for the longest time at this location, and because any eccentricity introduced at the jaw is amplified locally by the buckling. (A detailed analysis of a bar buckling from eccentric impact is given in the next chapter, along with a computer code that displays movies of the buckling bar for a variety of impact conditions and time frames specified by the user.) Nevertheless, the major features of the buckled form are similar to the idealization in Figure 1.1. We will see in the next chapter that the tendency for pulse buckling into a characteristic wavelength is a general feature of pulse buckling. It occurs because a band of “preferred” modes grows more rapidly than others. Their wavelengths depend on the pulse amplitude. This is another property of pulse buckling that sets it apart from vibration buckling: the modes of buckling depend on the load and must be determined as

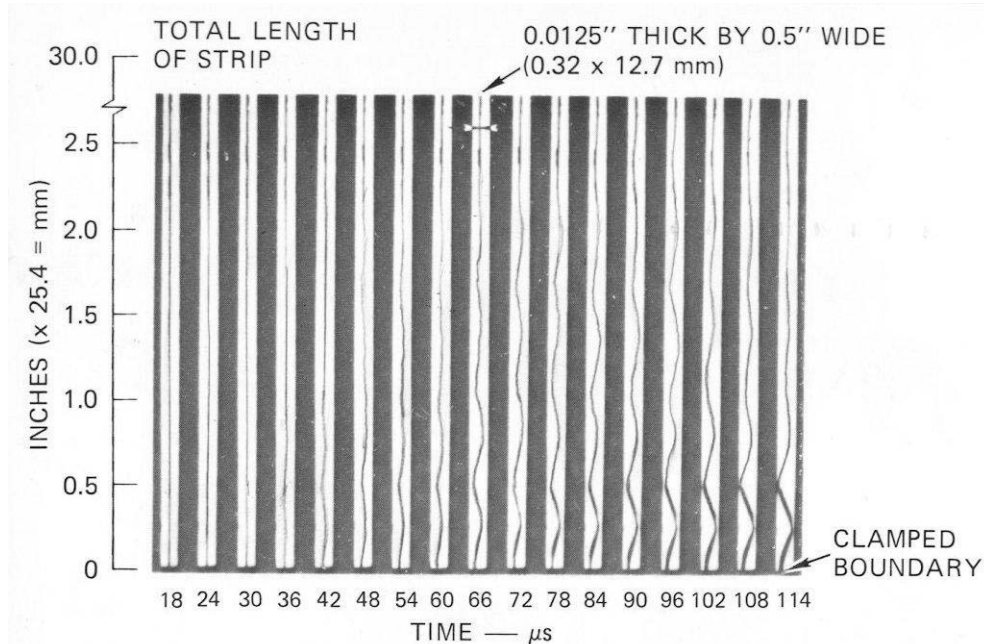


Figure 1.2: Waves forming in a 6061-T6 aluminum strip (time is measured from the instant a 40 ksi compressive wave reflects from the clamp support at the bottom).

part of the solution. This is distinct from static buckling, in which buckle modes are the lowest modes of response and can generally be determined independently from the buckle load amplitude.

Another example of pulse buckling is given in Figure 1.3. A sequence of framing camera photographs is given for a thin-walled cylindrical shell (radius-to-thickness ratio $a/h = 550$) impacted at its lower end (axial stress 1.5 times the classical static axial buckling stress). In this case the impact condition was produced by clamping the shell to a massive internal ring at its base (the top of an external clamping strap at the same location as the ring can be seen in the photographs) and suddenly projecting the ring upwards by an explosively-induced stress wave in a very massive anvil on which the ring was placed.

Ripples can be seen forming near the clamping ring in much the same way as in the bar example in Figure 1.2. However, in the shell the ripples are two-dimensional with clearly evident wavelengths in the circumferential as well as axial direction. At very late times the buckles take on the familiar post-buckled diamond shape of static buckling. However, the wavelengths of buckling are much shorter than the post-buckled shapes of static buckling, as shown in Figure 1.4 where this shell is compared with an identical shell buckled statically in a commercial testing machine.

Furthermore, the axial and circumferential wavelengths of the dynamic buckles, in both the high-speed and post-buckled photographs, are those calculated with classical linear buckling theory. The static post-buckled pattern has much longer wavelengths than the dynamic ones in both directions, because of complex nonlinear motion that follows the initial instability. This type of static buckling occurs in imperfection-sensitive structures,

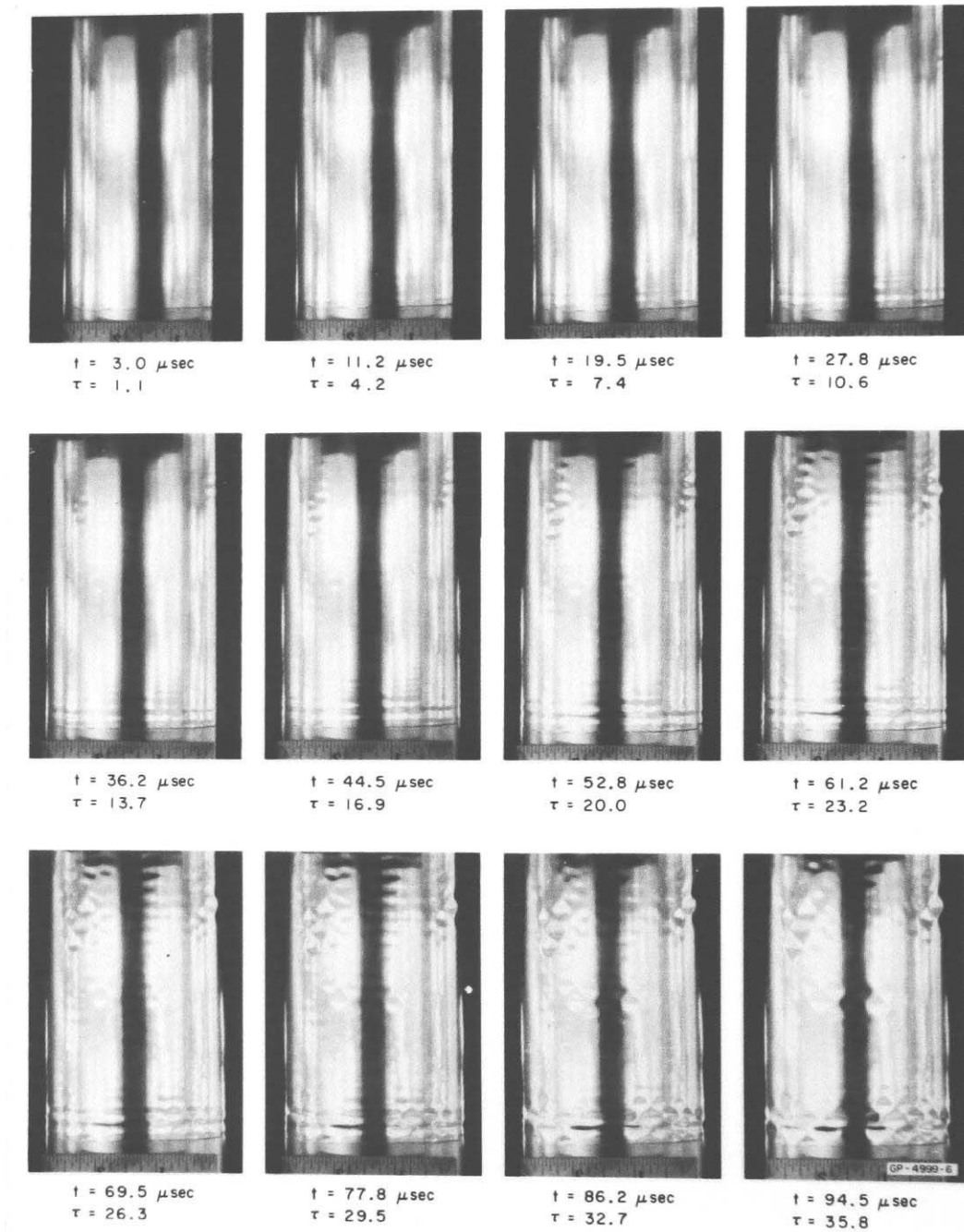


Figure 1.3: Ultra-high speed framing camera photographs of buckling in a thin cylindrical shell under axial impact. (Time is from initial impact at the rigid end ring whose clamping strap appears as a darkened area below a distinct line around the shell.)



Figure 1.4: Comparison of dynamic and static post-buckled patterns.

the cylindrical shell being the pre-eminent example.

This brings us to a third type of dynamic buckling: the lowering of static buckling loads because of the suddenness of an applied long-duration load. In this case both the static and suddenly-applied loads are substantially lower than the classical static linear-elastic buckling load. The dynamics of the nonlinear response are such that nonlinear buckling is precipitated at still lower loads than the static reduction caused by the nonlinearity. Analysis of this type of dynamic buckling is given in Chapter 4, along with treatment of the pulse buckling in Figure 1.4.

A fourth type of dynamic buckling must be considered in designing shaped charges and explosive pipe closures. The pipe closure problem is analyzed in Chapter 3. Accurately timed and very rapid closure of pipes is done by detonating an explosive charge placed around the pipe. As the pipe wall moves in there is a tendency for high-mode buckles to form that could interfere with the desired uniform wall collapse. This type of pulse buckling differs from those discussed above in that the load must be made intense enough to avoid buckling rather than low enough.

Many other types of dynamic buckling occur and have been reported in the Mechanics Literature. These will be noted but not considered further in this little book. One such type is flutter-enhanced bending and buckling. Bending deformations of the highly-stressed skin of aerospace vehicles are amplified by interaction with aerodynamic flow across the skin (Fung). Another type is snap-through of arches and domes. A key consideration in this type of instability is that deformation modes other than the post-snapped shape must

be included in the analysis. The arch or dome begins and ends in a symmetric shape, but goes from one to the other via asymmetric modes that allow the structure to wriggle from pre- to post-buckled shape with less strain energy than for a completely symmetric snap through. The list of dynamic instabilities goes on and on as one considers the variety of engineering structures encountered in practice. Another class of instability arises in the interaction of control systems and structural response.

The following three chapters focus on simple bars, rings and long cylindrical shells, and finite-length cylindrical shells with simple supports, because the theory of dynamic buckling reduces to its simplest forms in these structural elements. Our objective is to introduce various features of dynamic buckling with as few extraneous complexities as possible, so as to focus attention on learning the subject rather than its ramifications. The bar is obviously the simplest element because of its long history in the design of columns under static loading, for which the theory reduces to very fundamental form. A ring or long cylindrical shell under symmetric loading is simpler than the bar in the sense that the complexities of in-plane stress-wave propagation do not enter as in the bar under impact at one end. The simplest case of all is plastic-flow buckling of a ring, because for the typically small strain-hardening moduli of engineering metals the hoop stress can be treated as a constant yield stress throughout the ring. The ring is also the basic element in which to introduce buckle avoidance during dynamic plastic closure to a solid mass (the pipe closure problem). The cylindrical shell introduces two-dimensional buckle patterns in the simplest case and also imperfection-sensitive nonlinear static and dynamic buckling in which loads are constant of essentially infinite duration.

Chapter 2

Buckling of Simple Bars

This chapter is concerned mainly with dynamic elastic buckling of long bars from axial loads well in excess of the static Euler load of the bar considered as a simply supported column. In fact, in bar impact experiments of the type given in Figure 1.2, the bars are so long that they buckle before any signal is received from the free end, so there is no bar length and hence no physical Euler load. Nevertheless, it is useful to formulate the theoretical problem as though the bar were a column with supports at both ends because of the familiarity of this formulation and because it allows direct use of a statistical response analysis available from communication theory. Also, before we consider dynamic pulse buckling of this bar, it is useful to present the theory of static buckling. This helps by relating dynamic buckling to the more familiar static buckling problem.

2.1 Equations of Motion

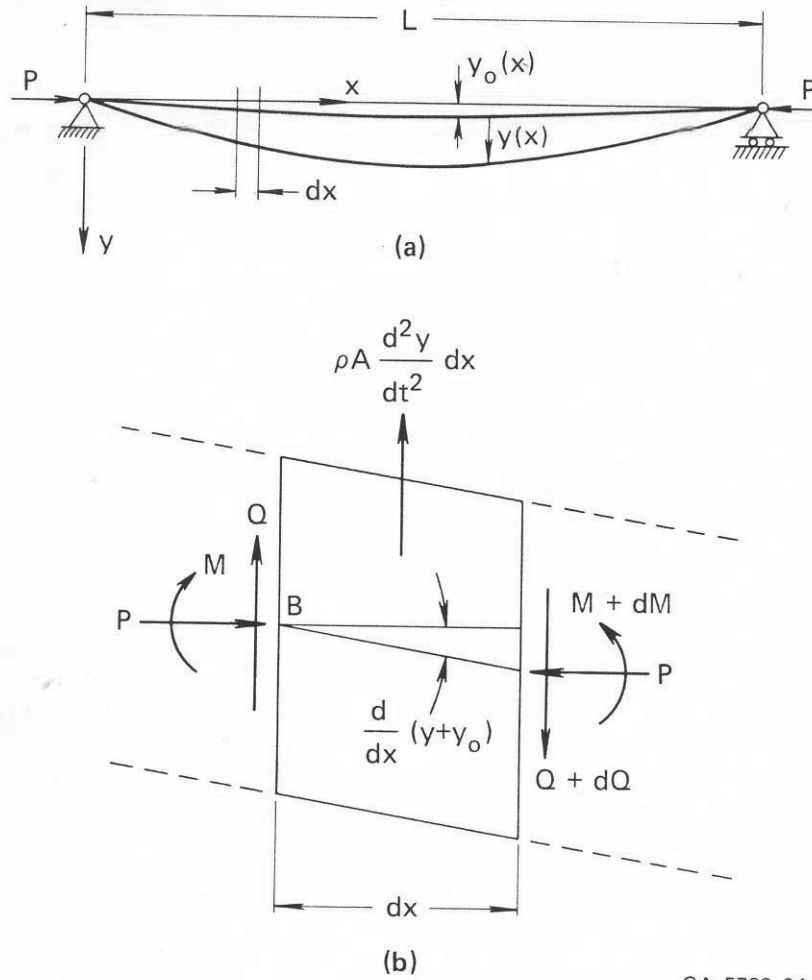
We consider elastic buckling of a simply supported uniform bar under axial compression as in Figure 2.1a. The bar has length L and supports an axial compressive force P . Its cross section is uniform with axial distance x , measured from one end. Deflection $y(x, t)$ is taken positive downward and is measured from an unstressed initial deflection $y_0(x)$. An element of length dx between two cross sections taken normal to the original (undeflected) axis of the bar is shown in Figure 2.1b. The shearing force Q and bending moment M acting on the sides of the element are taken positive in the directions shown. The inertia force acting on the element is $\rho A(\partial^2 y/\partial t^2)dx$, where ρ is the density of the bar material, A is the area of the cross section, and t is time.

The basic equations for the analysis of bar buckling are derived from dynamic equilibrium of the element in Figure 2.1b and the moment-curvature relation for the bar. Summation of forces in the y direction gives

$$-Q - \rho A \frac{\partial^2 y}{\partial t^2} dx + (Q + dQ) = 0$$

or

$$\rho A \frac{\partial^2 y}{\partial t^2} = \frac{dQ}{dx} \tag{2.1}$$



GA-5733-3A

Figure 2.1: Bar nomenclature and element of length.

Moments about point B and neglect of rotary inertia of the element results in

$$M - \rho A \frac{\partial^2 y}{\partial t^2} dx \frac{dx}{2} + (Q + dQ)dx - (M + dM) + P \frac{\partial}{\partial x}(y + y_0)dx = 0$$

Terms of second order are neglected to reduce this equation to

$$Q = \frac{\partial M}{\partial x} - P \frac{\partial}{\partial x}(y + y_0) \quad (2.2)$$

When the effects of shear deformations and shortening of the bar axis are neglected, the curvature of the bar axis is related to the bending moment by

$$EI \frac{\partial^2 y}{\partial x^2} = -M \quad (2.3)$$

in which E is Young's modulus and I is the moment of inertia of the bar section, assumed symmetric about the xy plane (otherwise the bar would twist in addition to bending). The differential equation for deflection of the bar axis is found by differentiating (2.2) and then eliminating Q by means of (2.1) and M by means of (2.3) twice differentiated. The result is

$$EI \frac{\partial^4 y}{\partial x^4} + P \frac{\partial^2}{\partial x^2}(y + y_0) + \rho A \frac{\partial^2 y}{\partial t^2} = 0 \quad (2.4)$$

2.2 Static Buckling

For static buckling, the inertia term is neglected and (2.4) becomes

$$EI \frac{d^4 y}{dx^4} + P \frac{d^2 y}{dx^2} = -P \frac{d^2 y_0}{dx^2}$$

or, with $k^2 = P/EI$,

$$\frac{d^4 y}{dx^4} + k^2 \frac{d^2 y}{dx^2} = -k^2 \frac{d^2 y_0}{dx^2} \quad (2.5)$$

We consider first a bar with no initial deflection, for which we need only the general solution to the homogeneous equation [with $y_0(x) \equiv 0$]:

$$y = A \sin kx + B \cos kx + Cx + D \quad (2.6)$$

For a simply supported bar the deflection and bending moment are zero at the ends and the boundary conditions are therefore

$$y = \frac{d^2 y}{dx^2} = 0 \quad \text{at} \quad x = 0 \quad \text{and} \quad x = L \quad (2.7)$$

Application of these conditions to (2.6) gives

$$B = C = D = 0, \quad \sin kL = 0$$

and therefore

$$kL = \pm n\pi$$

where n is an integer. By using the definition of k this becomes an equation for P .

$$P_n = \frac{\pi^2 EI}{L^2} \cdot n^2 \quad (2.8)$$

Thus, with no initial deflection only discrete values of P give a nontrivial solution, and the magnitude A of the deflection is undetermined.

Before discussing this solution further, let us treat the bar having an initial shape $y_0(x)$. The solution for the perfectly straight bar suggests that $y_0(x)$ should be expressed by the Fourier sine series

$$y_0(x) = \sum_{n=1}^{\infty} a_n \sin \frac{n\pi x}{L} \quad (2.9)$$

The coefficients in this series are found from

$$a_n = \frac{2}{L} \int_0^L y_0(x) \sin \frac{n\pi x}{L} dx \quad (2.10)$$

Substitution of (2.9) into (2.5) gives the following differential equation for the imperfect bar:

$$\frac{d^4 y}{dx^4} + k^2 \frac{d^2 y}{dx^2} = k^2 \frac{n^2 \pi^2}{L^2} \sin \frac{n\pi x}{L} \quad (2.11)$$

To find a particular solution we take

$$y_p = \sum_{n=1}^{\infty} A_n \sin \frac{n\pi x}{L} \quad (2.12)$$

When this is substituted into (2.11) the coefficients are found to be

$$A_n = \frac{-k^2 a_n}{k^2 - n^2 \pi^2 / L^2} = \frac{-P a_n}{P - P_n} \quad (2.13)$$

The complete solution is then

$$y = A \sin kx + B \cos kx + Cx + D - \sum_{n=1}^{\infty} \frac{P a_n}{P - P_n} \sin \frac{n\pi x}{L} \quad (2.14)$$

Since P , and hence k , is arbitrary, application of the boundary conditions (2.7) gives $A = B = C = D = 0$, and the general solution is simply

$$y = - \sum_{n=1}^{\infty} \frac{P a_n}{P - P_n} \sin \frac{n\pi x}{L} \quad (2.15)$$

From this solution we see that the deflection becomes arbitrarily large as P approaches the critical loads P_n given by (2.8). However, the dynamic solution given in subsequent sections shows that the motion is unstable for *any* load greater than the lowest critical load P_1 , which, from (2.8), is given by

$$P_1 = \frac{\pi^2 EI}{L^2} \quad (2.16)$$

In the neighborhood of $P = P_1$ the first term dominates the deflection. By reasonably neglecting the higher terms, the midspan deflection for $P < P_1$ is given approximately by

$$\delta = y(L/2) \approx \frac{-P a_1}{P - P_1} \quad (2.17)$$

Figure 2.2 gives a plot of deflection δ from (2.17) versus end load P . On the basis of this formula, Southwell suggested that the critical load P_1 could be extracted from test data by plotting δ/P versus δ . In this form (2.17) becomes

$$\frac{\delta}{P} = \frac{1}{P_1}(\delta + a_1) \quad (2.18)$$

which gives the straight line in the right hand graph of Figure 2.2. The inverse of the slope gives the critical load P_1 and the δ intercept gives the coefficient a_1 as shown.

If the bar is treated as initially perfectly straight but subjected to an eccentrically placed load, the Southwell procedure can still be used to determine the critical load. Consider, for example, that the load is displaced from the centroidal axis by an amount ϵ , equal at both ends. This can be treated as a bar having an initial displacement given by

$$y_0(x) = \begin{cases} \epsilon & x \neq 0, L \\ 0 & x = 0, L \end{cases} \quad (2.19)$$

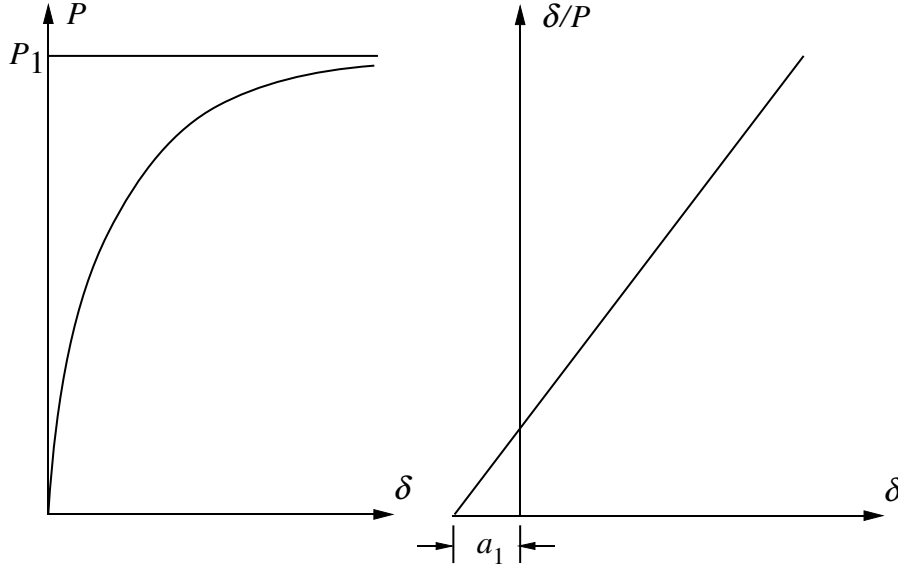


Figure 2.2: Force-deflection curve and Southwell plot.

When this displacement is substituted into (2.10) the coefficient of the first term in its Fourier expansion is found to be

$$a_1 = \frac{4\epsilon}{\pi} \quad (2.20)$$

Thus, for P in the neighborhood of P_1 the Southwell plot is as described previously and the δ intercept is now $4\epsilon/\pi$. If the bar is considered to have both an initial shape imperfection and some eccentricity, (2.18) becomes

$$\frac{\delta}{P} = \frac{1}{P_1} \left\{ \delta + \left(a_1 + \frac{4\epsilon}{\pi} \right) \right\} \quad (2.21)$$

For real columns, in which both a_1 and ϵ are small and difficult to measure, there is therefore no way of telling in a Southwell plot how much of the deflection is caused by load eccentricity and how much is caused by an initial deflection. In experiments run a century ago it was found that the experimental buckling deflections could be calculated, on average, by using values of equivalent eccentricity given by

$$\epsilon = 0.06r^2/d \quad (2.22)$$

where r^2/d is the core radius of the cross section, r being the radius of gyration and d the distance from the elastic axis to the outermost fiber. For a rectangular bar of depth h the core radius is $h/6$ and $\epsilon = 0.01h$. In long columns it is reasonable to assume that the initial imperfections in shape will take on increased importance, and these can be expected to depend on the length of the column. On this basis, Salmon found that, although equivalent imperfections from a large collection of experimental results were scattered by an order of magnitude at any given length, both the average amplitude of the imperfections and the range of amplitudes increased in proportion to the length of the

bars. For the longer columns almost all imperfections were in the band

$$0.0001 < \frac{a_1}{L} < 0.001 \quad (2.23)$$

Several authors have proposed that imperfections depending on both the core radius and the column length can be expected to be present. They suggest that a conservative estimate for an equivalent deflection including both types of imperfections can be taken as

$$a_1 = 0.1 \frac{r^2}{d} + \frac{L}{750} \quad (2.24)$$

In the dynamic problems discussed in later sections we will see that the range of normalized imperfections found in static buckling are in reasonably good agreement with values observed in dynamic buckling, with attention focused on the shorter wavelengths of dynamic buckling.

2.3 Theory for Dynamic Buckling

The static buckling considered in the preceding sections was concerned with the steady load that can be safely carried by a column or bar. If, instead, a load is suddenly applied and then removed, as in an air hammer impacting concrete, the maximum load can far exceed the static buckling load without inducing objectionably large bending strains or deflections. Because of this feature in the dynamic problem, rather than seeking the maximum load that can be carried we specify a load and seek the response. Knowing how the buckling grows with time we then determine the maximum duration for which the given load can be applied safely.

Consider first the same load and bar as just analyzed for static buckling, except that now the magnitude of P can be very much larger than the static Euler load P_1 . To keep the bar from buckling during application of the load imagine that it is supported along its entire length by lateral constraining blocks.¹ Then, at time $t = 0$, the blocks are suddenly removed and buckling motion begins. The motion is governed by Equation (2.4), repeated here for ease of reading:

$$EI \frac{\partial^4 y}{\partial x^4} + P \frac{\partial^2}{\partial x^2} (y + y_0) + \rho A \frac{\partial^2 y}{\partial t^2} = 0 \quad (2.25)$$

After dividing through by EI it is convenient to introduce the parameters

$$k^2 = \frac{P}{EI} \quad r^2 = \frac{I}{A} \quad c^2 = \frac{E}{\rho} \quad (2.26)$$

The first two parameters have already appeared in the static problem. The new parameter c , appearing because of the dynamic inertia term, is the wave speed of axial stress waves in the bar. When these quantities are used the equation of motion (2.25) becomes

$$\frac{\partial^4 y}{\partial x^4} + k^2 \frac{\partial^2 y}{\partial x^2} + \frac{1}{r^2 c^2} \frac{\partial^2 y}{\partial t^2} = -k^2 \frac{\partial^2 y_0}{\partial x^2} \quad (2.27)$$

¹In practice, the load is suddenly communicated to the bar by an axial stress wave (or waves). Effects of these waves are small, as will be seen in Section 2.9.

As in the static problem the boundary conditions of zero moment and displacement at the ends of the bar give

$$y = \frac{\partial^2 y}{\partial x^2} = 0 \quad \text{at} \quad x = 0 \quad \text{and} \quad x = L \quad (2.28)$$

The solution to (2.27) subject to boundary conditions (2.28), as in the static problem, can be expressed by a Fourier sine series in x . Thus, we take a product solution

$$y(x, t) = \sum_{n=1}^{\infty} q_n(t) \sin \frac{n\pi x}{L} \quad (2.29)$$

The initial displacement $y_0(x)$ is also expressed in series form

$$y_0(x) = \sum_{n=1}^{\infty} A_n \sin \frac{n\pi x}{L} \quad (2.30)$$

where the coefficients are found with

$$A_n = \frac{2}{L} \int_0^L y_0(x) \sin \frac{n\pi x}{L} \quad (2.31)$$

Equations (2.29) and (2.30) are now substituted into (2.27) to give the following equation of motion for the Fourier coefficients $q_n(t)$

$$\left[\frac{n^4 \pi^4}{L^4} - k^2 \frac{n^2 \pi^2}{L^2} \right] q_n + \frac{1}{r^2 c^2} \ddot{q}_n = k^2 \frac{n^2 \pi^2}{L^2} A_n \quad (2.32)$$

which upon rearranging to the more standard form becomes

$$\ddot{q}_n + \frac{r^2 c^2 n^2 \pi^2}{L^2} \left[\frac{n^2 \pi^2}{L^2} - k^2 \right] q_n = r^2 c^2 k^2 \cdot \frac{n^2 \pi^2}{L^2} A_n \quad (2.33)$$

One of the principle points of the theory of pulse buckling appears here. The nature of the solutions to (2.33) depends on the sign of the coefficient of q_n . If $n\pi/L < k$ this coefficient is negative and the solutions are hyperbolic; if $n\pi/L > k$ this coefficient is positive and the solutions are trigonometric. Thus, if the mode numbers n are large enough, i.e., $n > kL/\pi$, the displacements are trigonometric and therefore bounded. However, over the lower range of mode numbers, $n < kL/\pi$, the hyperbolic solutions grow exponentially with time and have the potential of greatly amplifying small initial imperfections. These modes are therefore called the *buckling modes*.

The mode number $n = kL/\pi$ that separates the trigonometric and hyperbolic solutions gives a wavelength corresponding to the wavelength of static buckling under the given load P ; no matter how long the duration of load application, if $n > kL/\pi$ the motion remains bounded, while for any $n < kL/\pi$ the motion diverges. To see more clearly this relationship with a static buckling problem, recall first from (2.29) that the deflection curve of the bar is a sine wave with n half-waves. For $n = kL/\pi$ this curve is given by

$\sin kx$. One half-wave of this deflection curve, corresponding to the buckle shape of a simple pinned Euler column, therefore occupies a distance from the left support given by

$$kx_{\text{st}} = \pi$$

or

$$x_{\text{st}} = \pi/k \quad (2.34)$$

By applying the definition $k^2 = P/EI$ this equation becomes

$$P = \frac{\pi^2 EI}{x_{\text{st}}^2} \quad (2.35)$$

This is identical to (2.16) for the static buckling of an Euler column of length x_{st} under load P .

The dynamic equation also demonstrates the statement made in Section 2.2 that any load greater than $P_1 = \pi^2 EI/L^2$, not just the eigenvalues of the static problem, gives unstable motion. This follows from the observation already made that the motion is unstable if the coefficient of q_n in (2.33) is negative, that is, if

$$\frac{n^2 \pi^2}{L^2} - k^2 < 0 \quad (2.36)$$

Since $k^2 = P/EI$ is positive, this quantity is most negative for $n = 1$. With $n = 1$ in (2.36) the left-hand side is negative for all $P > \pi^2 EI/L^2$ and the motion is unstable as previously stated.

For the dynamic problems of present interest, $P \gg \pi^2 EI/L^2$ and many modes are unstable. The mode numbers of the buckling modes are therefore very high and the wavelengths so short that the total length of the bar becomes unimportant except as it affects axial loading. In fact, in experiments to be described later, dynamic buckling is produced by impact at one end of the bar and, because of the finite speed of axial wave propagation, buckling occurs before any signal is received from the opposite end. In this problem the total length of the bar has no significance at all. We should therefore seek a characteristic length other than the length of the bar. Because the nature of the motion changes at the static Euler wavelength $x_{\text{st}} = \pi/k$, it is natural to use $1/k$ as the characteristic length in the x -direction, along the bar. Similarly, it is natural to normalize lateral deflections with respect to the radius of gyration r of the cross section. The ratio of these lengths is a significant parameter and will be denoted by s .

$$s^2 = r^2 k^2 = \frac{r^2 P}{EI} = \frac{P}{AE} = \epsilon \quad (2.37)$$

Thus the buckling wavelengths vary inversely with the square root of the strain ϵ from the compression load P . This will be discussed more fully later.

To incorporate these lengths into the equation of motion, we introduce the dimensionless variables

$$w = \frac{y}{r} \quad \xi = kx = \frac{sx}{r} \quad \tau = \frac{s^2 ct}{r} \quad (2.38)$$

With these variables (2.25) becomes

$$w'''' + w'' + \ddot{w} = w_0'' \quad (2.39)$$

where primes indicate differentiation with respect to ξ and dots indicate differentiation with respect to τ . Boundary conditions (2.28) become

$$w = w'' = 0 \quad \text{at} \quad \xi = 0 \quad \text{and} \quad \xi = \ell = \frac{sL}{r} \quad (2.40)$$

and the product form of the solution is now expressed by

$$w(\xi, \tau) = \sum_{n=1}^{\infty} g_n(\tau) \sin \frac{n\pi\xi}{\ell} \quad (2.41)$$

Similarly, the initial displacements become

$$w_0(\xi) = \sum_{n=1}^{\infty} a_n \sin \frac{n\pi\xi}{\ell} \quad (2.42)$$

where

$$a_n = \frac{2}{\ell} \int_0^{\ell} w_0(\xi) \sin \frac{n\pi\xi}{\ell} d\xi \quad (2.43)$$

A wave number η is introduced by

$$\eta = \frac{n\pi}{\ell} \quad (2.44)$$

and finally (2.41) and (2.42) are substituted into (2.39) to give the equations of motion for the Fourier coefficients $g_n(\tau)$.

$$\ddot{g}_n + \eta^2(\eta^2 - 1)g_n = \eta^2 a_n \quad (2.45)$$

This corresponds to (2.33); in the new notation the transition from hyperbolic to trigonometric solutions occurs at $\eta = 1$.

The general solution to (2.45) is

$$g_n(\tau) = C_n \cosh p_n \tau + D_n \sinh p_n \tau - \frac{a_n}{1 - \eta^2} \quad \text{for } \eta < 1 \quad (2.46)$$

$$g_n(\tau) = C_n \cos p_n \tau + D_n \sin p_n \tau - \frac{a_n}{1 - \eta^2} \quad \text{for } \eta > 1$$

where

$$p_n = \eta|1 - \eta^2|^{1/2}$$

These equations are substituted into (2.41) to obtain the general solution for lateral displacement.

$$\begin{aligned} w(\xi, \tau) = & \sum_{n=1}^N \left[C_n \cosh p_n \tau + D_n \sinh p_n \tau - \frac{a_n}{1 - \eta^2} \right] \sin \frac{n\pi\xi}{\ell} \\ & + \sum_{n=N+1}^{\infty} \left[C_n \cos p_n \tau + D_n \sin p_n \tau - \frac{a_n}{1 - \eta^2} \right] \sin \frac{n\pi\xi}{\ell} \end{aligned} \quad (2.47)$$

where N is the largest integer for which $\eta < 1$.

The bar is assumed to be initially at rest. Also, recall that w is measured from the initial displacement w_0 , so the initial conditions are

$$w(\xi, 0) = \dot{w}(\xi, 0) = 0 \quad (2.48)$$

Application of these to (2.47) yields $D_n = 0$ and $C_n = a_n/(1 - \eta^2)$. The final solution is then

$$w(\xi, \tau) = \sum_{n=1}^{\infty} \frac{a_n}{1 - \eta^2} \left[\frac{\cosh p_n \tau - 1}{\cos p_n \tau} \right] \sin \frac{n\pi\xi}{\ell} \quad (2.49)$$

in which the hyperbolic form is taken for $\eta < 1$ and the trigonometric form for $\eta > 1$.

2.4 Amplification Functions

Equation (2.49) shows qualitatively the exponential growth of the buckling terms. The ratio between the Fourier coefficients a_n of the initial displacement and the coefficients $g_n(\tau)$ as the structure buckles will be called the *amplification function* and in this problem is given by

$$G_n(\tau) = \frac{g_n(\tau)}{a_n} = \begin{cases} \frac{1}{1 - \eta^2} \left[\frac{\cosh p_n \tau - 1}{\cos p_n \tau} \right] & \text{if } \eta \neq 1 \\ \tau^2/2 & \text{if } \eta = 1 \end{cases} \quad (2.50)$$

A plot of this function, treating η as a continuous variable, is given in Figure 2.3 for values of dimensionless time τ that span from significant amplification occurring for a range of both trigonometric and hyperbolic modes ($\tau = 2$ and 4) to the onset of amplification being dominated by the hyperbolic modes $\eta < 1$ (at $\tau = 6$). Experiments show that nonlinear effects, such as onset of plastic hinges, begin at $\tau \approx 8$. This can be taken as a first-order criterion for critical loads at the onset of pulse buckling. For a given structure, specification of $\tau = 8$ can be used to calculate combinations of load amplitude and duration that cause buckling. In fact, from the definitions of s and τ in (2.37) and (2.38) τ is proportional to the applied impulse.

It is apparent that as time increases a narrowing band of wavelengths is amplified having wave numbers centered at somewhat less than $\eta = 1$. To find the wave number of the most amplified mode for late times we differentiate (2.50) for $\eta < 1$.

$$\frac{dG_n}{d\eta^2} = \frac{(1 - 2\eta^2)}{2\eta^2(1 - \eta^2)^2} \cdot p_n \tau \sinh p_n \tau + \frac{1}{(1 - \eta^2)^2} (\cosh p_n \tau - 1) \quad (2.51)$$

Setting this to zero yields

$$1 - \frac{1}{2\eta^2} = \frac{1}{p_n \tau} \cdot \frac{\cosh p_n \tau - 1}{\sinh p_n \tau} \quad (2.52)$$

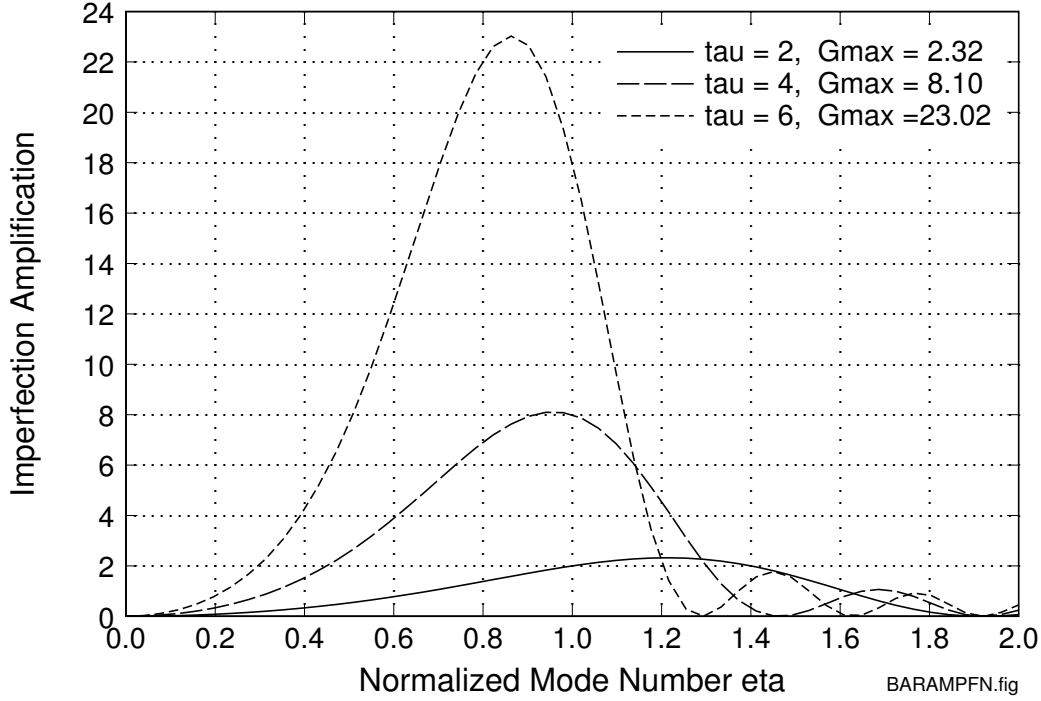


Figure 2.3: Amplification Function.

For times large enough that significant amplification has occurred, $\cosh p_n \tau - 1 \approx \sinh p_n \tau$ and (2.52) is approximated by

$$\eta_{cr}^2 = \frac{p_n \tau}{2(p_n \tau - 1)} \quad (2.53)$$

To a lesser approximation for large τ such that $p_n \tau \gg 1$, the wave number of the most amplified mode is therefore

$$\eta_{cr} \approx 1/\sqrt{2} = 0.707 \quad (2.54)$$

With this used to obtain an estimate for $p_{cr} = \eta_{cr}(1 - \eta_{cr})^{1/2} \approx 1/2$, a better estimate for η_{cr} , from (2.53), is

$$\eta_{cr} \approx \frac{1}{\sqrt{2}} \cdot \sqrt{\frac{\tau}{\tau - 2}} \quad (2.55)$$

For example, at $\tau = 6$, (2.55) gives $\eta_{cr} = 0.866$, which is about 22% larger than the value in (2.54). At $\tau = 10$ the equation gives $\eta_{cr} = 0.791$ and at $\tau = 12$ it gives $\eta_{cr} = 0.775$. Thus, to a rough approximation the wave number of the most amplified mode can be taken as simply $\eta_{cr} \approx \eta_p \equiv 0.8$. This will be called the “preferred” mode of buckling. The corresponding wavelength is found from

$$\eta_p \xi_p = 2\pi, \quad \text{or} \quad \xi_p \equiv \lambda_p = 2\pi/0.8 = 7.85 \quad (2.56)$$

In dimensional units, from (2.38), this length is

$$x_p = \frac{r}{s} \lambda_p = \frac{2\pi}{0.8\sqrt{\epsilon}} \cdot r = 7.85 r/\sqrt{\epsilon} \quad (2.57)$$

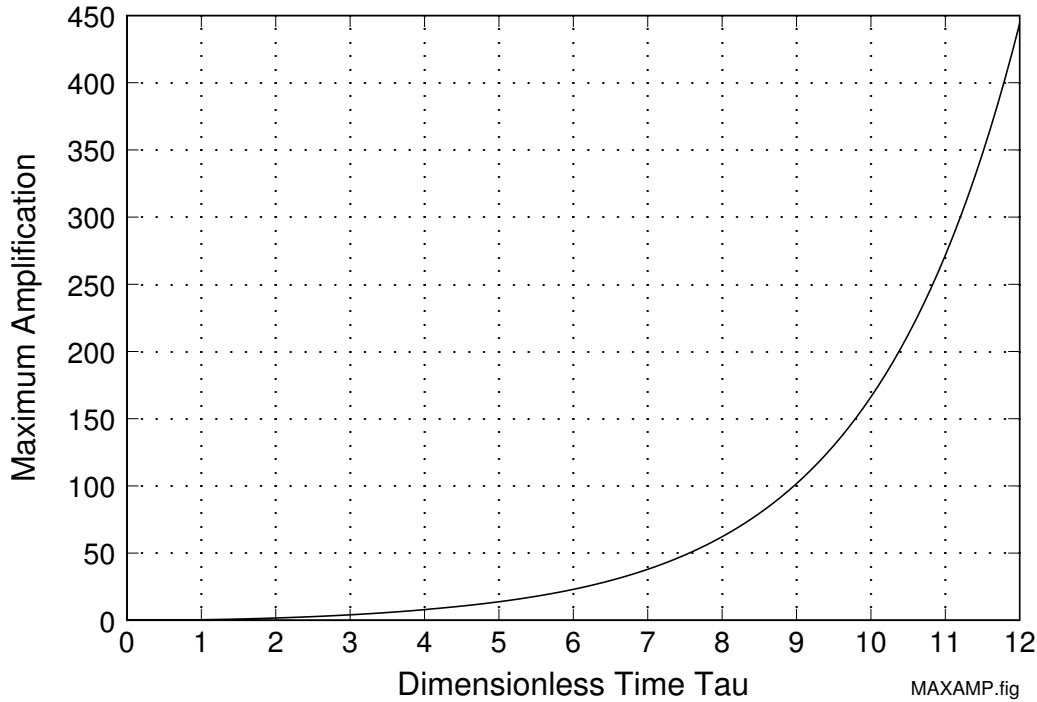


Figure 2.4: Maximum amplification versus dimensionless time.

A graph of the maximum amplification plotted against τ is given in Figure 2.4. Beyond $\tau = 4$ growth is very rapid; at $\tau = 12$ initial imperfections are amplified by more than 400. These results suggest that a bar under very high compression will buckle into wavelengths near $7.85 r/\sqrt{\epsilon}$ at dimensionless times between 5 and 10. (It is useful to note that in this graph, and any others that have dotted grid lines, the dots are spaced to provide accurate, round number, rulers that allow values to be read to an accuracy of about 1%. This is one of the advantages of writing your own graphics software!)

2.5 Pulse Buckling Under Eccentric Load

As an example, consider a bar eccentrically loaded by an uniform axial load P displaced from the bar centroid by eccentricity δ . The initial shape of the bar, measured from the centroid axis, is then

$$w_0(\xi) = \begin{cases} \delta/r & \xi \neq 0 \\ 0 & \xi = 0 \end{cases} \quad (2.58)$$

This shape is expanded into the Fourier sine series

$$w_0(\xi) = \sum_{n=1}^{\infty} a_n \sin \frac{n\pi\xi}{\ell} \quad (2.59)$$

The coefficients are found by using formula (2.43), which yields

$$a_n = \begin{cases} \frac{4\delta}{n\pi r} & \text{n odd} \\ 0 & \text{n even} \end{cases} \quad (2.60)$$

From (2.49) the buckled shape is given by

$$w(\xi, \tau) = \sum_{n=1,3,\dots}^{\infty} \frac{4\delta}{n\pi r} \cdot \frac{1}{1-\eta^2} \left[\frac{\cosh p_n \tau}{\cos p_n \tau} - 1 \right] \sin \frac{n\pi \xi}{\ell} \quad (2.61)$$

This solution is used in a small computer code to calculate and display buckle shapes at a sequence of times for various ranges of τ and various display amplitude resolutions. Buckling is displayed as a movie for each set of parameters specified by the user. A copy of the code is included with the electronic distribution of this little book. Before discussing how to use the code and interpret its results, we continue here to derive an approximate analytical solution for values of τ centered at about $\tau = 6$. This allows us to use specified physical conditions to derive critical buckling loads.

To obtain a simple formula for the buckling shapes given by (2.61), first recall that

$$\eta = \frac{n\pi}{\ell}; \quad \text{and therefore, for } n \text{ odd,} \quad \Delta\eta = \frac{2\pi}{\ell} \quad (2.62)$$

Then

$$\frac{4\delta}{n\pi r} = \frac{4\delta}{\eta \ell r} = \frac{4\delta}{r\eta} \cdot \frac{1}{2\pi} \cdot \frac{2\pi}{\ell} = \frac{2\delta}{\pi r \eta} \Delta\eta \quad (2.63)$$

and (2.61) can be written

$$w(\xi, \tau) = \frac{2\delta}{\pi r} \sum_{n=1,3,\dots}^{\infty} \frac{1}{\eta(1-\eta^2)} \left[\frac{\cosh p_n \tau}{\cos p_n \tau} - 1 \right] \sin \eta \xi \Delta\eta \quad (2.64)$$

If we assume that the bar is very long compared with the buckling wavelengths (long, thin bar under high-stress impact loads), $\Delta\eta \rightarrow d\eta$ and η can be treated as a continuous variable. The sum (2.64) can then be replaced by the integral

$$w(\xi, \tau) = \frac{2\delta}{\pi r} \int_0^{\infty} \frac{1}{\eta(1-\eta^2)} \left[\frac{\cosh p_n \tau}{\cos p_n \tau} - 1 \right] \sin \eta \xi \, d\eta \quad (2.65)$$

A plot of the function

$$f(\eta, \tau) = \frac{1}{\eta(1-\eta^2)} \left[\frac{\cosh p_n \tau}{\cos p_n \tau} - 1 \right] \quad (2.66)$$

in the integrand is given in Figure 2.5 for $\tau = 6$. To obtain an approximate analytical expression for the integral in (2.65) we replace this curve by the triangle of height A in the figure, where $A(\tau) = f(0.8, \tau)$. The value $\eta = 0.8$ corresponds to the peak of the Fourier

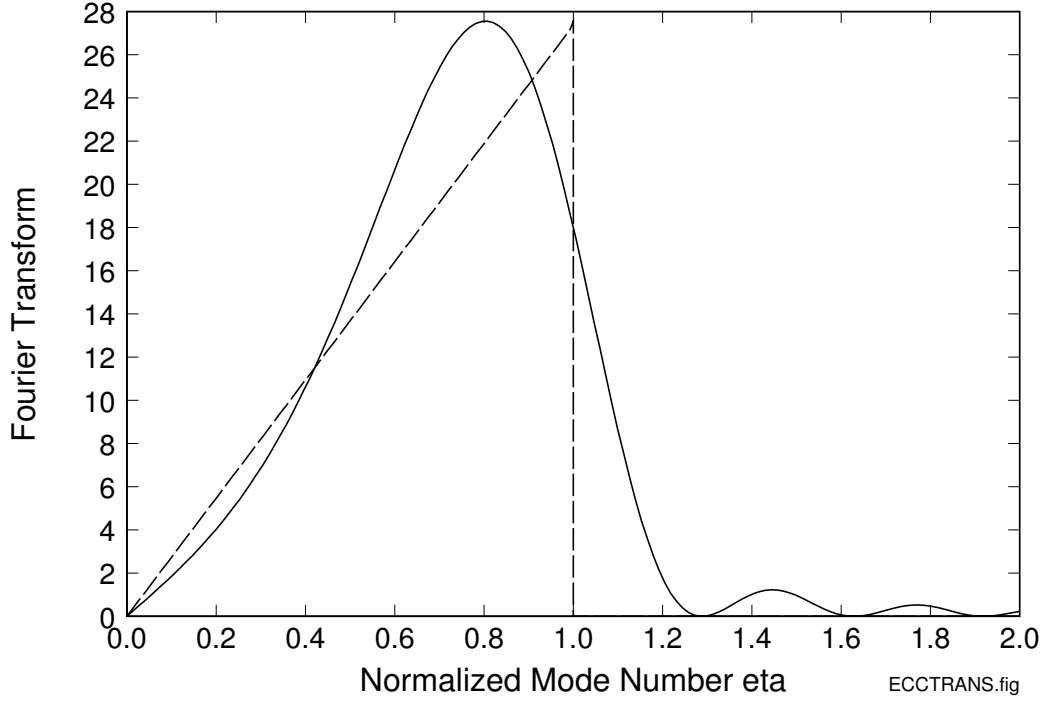


Figure 2.5: Fourier coefficients (transform) of buckle shape.

transform in Figure 2.5, and from the previous discussion, the peak of the transform for other values of τ near $\tau = 6$. Then

$$\begin{aligned}
 w(\xi, \tau) &\approx \frac{2\delta}{\pi r} \int_0^1 A(\tau) \eta \sin \eta \xi \, d\eta = \frac{2\delta A(\tau)}{\pi r \xi^2} (\sin \eta \xi - \eta \xi \cos \eta \xi) \Big|_0^1 \\
 &= \frac{2\delta A(\tau)}{\pi r \xi^2} (\sin \eta - \xi \cos \eta)
 \end{aligned} \tag{2.67}$$

where

$$A(\tau) = \frac{1}{0.8(1 - 0.8^2)} (\cosh 0.48 \tau - 1) \tag{2.68}$$

The function

$$W(\xi) = \frac{1}{\xi^2} (\sin \xi - \xi \cos \xi), \tag{2.69}$$

which gives the approximate shape of the buckling bar, is plotted in Figure 2.6. The wavelengths between peaks are slightly larger than 2π near the support and approach 2π away from the support.

This discussion gives an estimate for the buckled shape of a bar under eccentric thrust and also shows how the amplitude of the buckled form grows with time. Specification of a criterion for failure by dynamic buckling, however, depends on the particular structural problem at hand. For example, if the bar is a push rod used to measure rapid displacements, large deflections within the elastic limit could constitute failure. If a bar is used

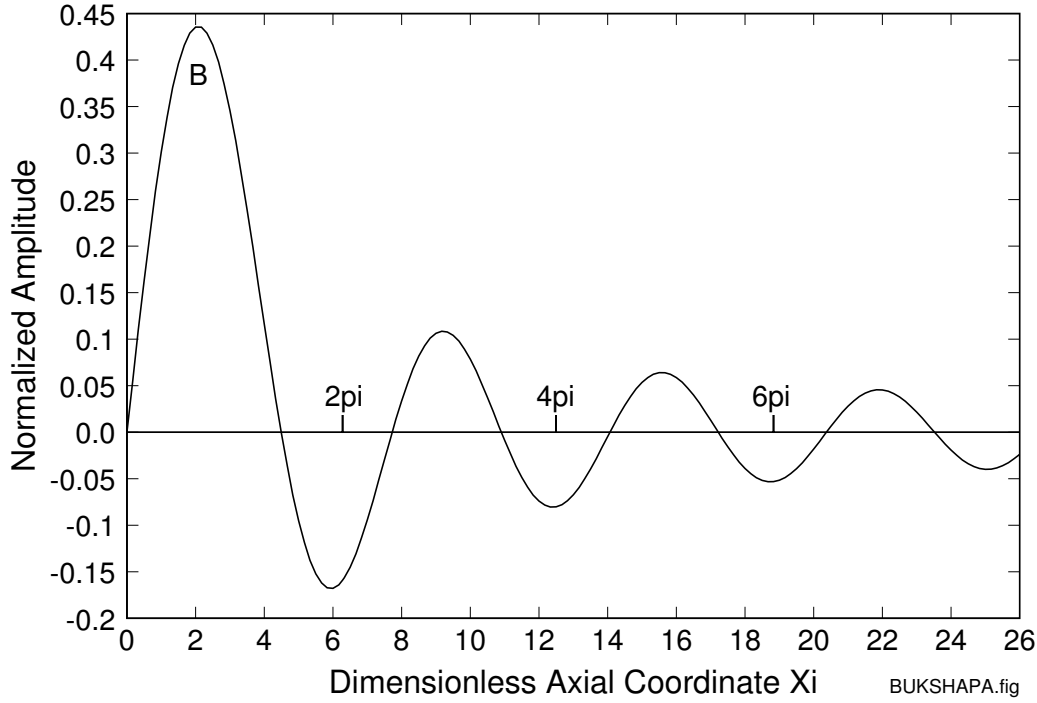


Figure 2.6: Approximate buckle shape of bar under suddenly applied eccentric load.

as a hammer, or is a long pile being driven into the soil, large displacements are probably not objectionable so long as the motion remains elastic and the bar returns to its initial shape.

To give a concrete example, let us calculate the duration of load application required to produce a combined bending-compression stress equal to the yield stress. The maximum bending stress occurs at point B in Figure 2.6 where the maximum curvature is $W'' = -0.235$. In general, the compressive bending stress in the concave outer fiber for a rectangular bar of height h is

$$\sigma_b = \frac{M(h/2)}{I} = \frac{Eh}{2} \frac{\partial^2 y}{\partial x^2} = \frac{Eh s^2}{2 r^2} r w'' = \sqrt{3} E s^2 w'' \quad (2.70)$$

With $W'' = -0.235$ substituted into (2.67) and the time variation from (2.68), the bending stress at B is

$$\sigma_b = \sqrt{3} E s^2 \frac{2\delta A(\tau)}{\pi r} (-0.235) = 0.900 \cdot \frac{\delta}{r} \cdot \sigma_c (\cosh 0.48\tau - 1) \quad (2.71)$$

where σ_c is the compressive impact stress.

The threshold of buckling is defined by the total stress $\sigma_b + \sigma_c$ reaching the yield stress σ_y . With σ_b from (2.71) this condition gives the following relation between the compressive stress σ_c and the time τ_{cr} at which yield occurs:

$$\frac{\sigma_y}{\sigma_c} = 1 + 0.900 \cdot \frac{\delta}{r} \cdot (\cosh 0.48\tau - 1) \quad (2.72)$$

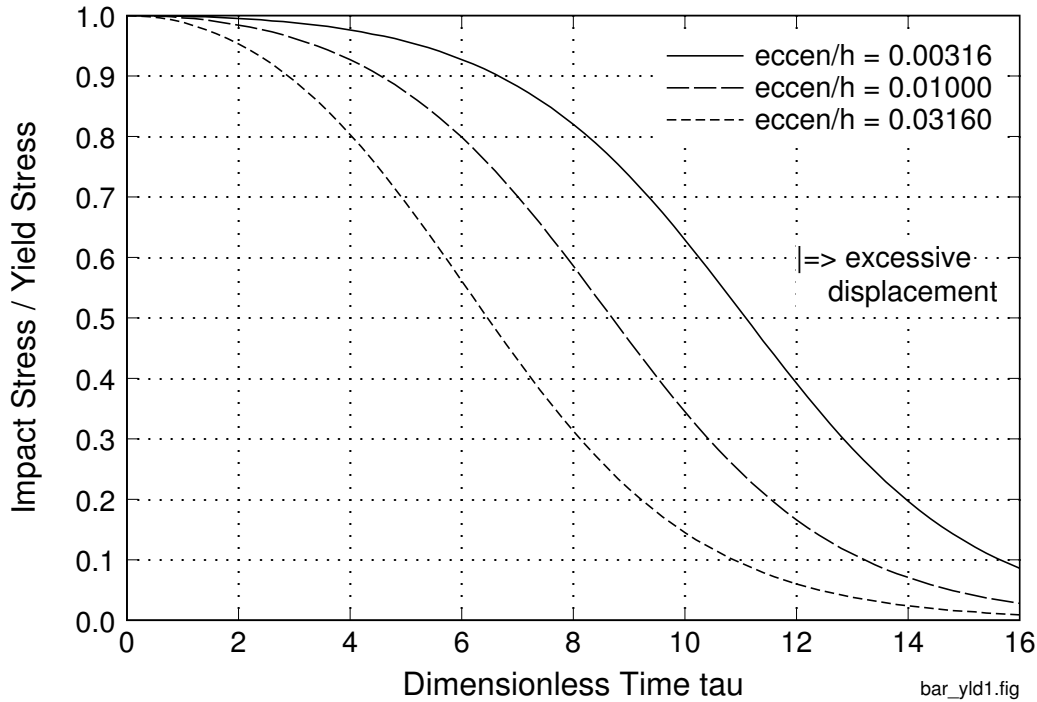


Figure 2.7: Critical impact stress versus impact duration to produce threshold yield in a bar under eccentric axial impact.

A graph of σ_c/σ_y versus τ_{cr} from (2.72) is given in Figure 2.7 for three values of eccentricity δ , with δ expressed as a multiple of depth h of a rectangular bar. The values chosen range over an order of magnitude, from $\delta = 0.00316 h$ to $\delta = 0.0316 h$, selected so these limits are the same factor up or down from a mid-value $\delta = 0.01 h$, a representative value found in static experiments as given in Equation (2.22). We shall see that the impact dynamic buckling experiments described in Section 2.8 suggest that the static data do indeed give imperfections in the appropriate range for the dynamic problem. Threshold yield data from the impact buckling experiments fall between the two dashed curves in Figure 2.7, giving equivalent eccentricities in the range $0.01 < \delta/h < 0.03$.

About 60 experiments were performed with axial stresses between 0.3 and 0.8 times the yield stress. None of the bars with data points to the left of the $\delta/h = 0.0316$ curve were buckled, and all of the bars with data points to the right of the $\delta/h = 0.01$ curve were buckled. Some of the bars with data points between these two curves were buckled and some were not, characteristic of the random nature of the imperfections. We can therefore take these two dashed curves as a band that specifies loads that produce threshold yield from buckling. Note that with very low impact stresses the critical loading times τ_{cr} become fairly large. The upper side of the band (the center curve in the graph) gives $\tau_{cr} = 13.2$ for $\sigma_c/\sigma_y = 0.1$. This value, entered into the amplification function in (2.50) with the wave number η from (2.55) for maximum amplification, gives a maximum modal amplification of 802. With the eccentricity $0.01 h$ at this upper side of the band the maximum modal amplitude is $8 h$, which is most likely too large to be acceptable. Thus,

while the curves in Figure 2.7 are plotted to $\tau = 16$ to show their nature toward this extreme, values above $\tau \approx 12$ would exceed a maximum displacement failure criterion.

2.6 Buckling Movies with a DOS code

A small computer code that runs on a PC in a Microsoft DOS window was written to calculate and display buckle shapes at a sequence of times.² This was done with the modal solution in (2.61), not the approximate solution in (2.67). Buckle amplitudes were normalized by the eccentricity, axial distance was expressed as the dimensionless ξ , and time was expressed as the dimensionless time τ . In this form the results are completely general and response depends only on τ , as we have seen in the preceding analyses.

Because the buckling depends only on τ , there is only one movie to display. However, the nature of the motion changes depending on the range of τ on which attention is focused. The code therefore allows the user to focus on either large or smaller values of τ and automatically adjusts the magnification of the displayed shape to use the entire screen at the final value of τ . Thus, if one selects a small range, for example to $\tau_{\max} = 2$, the maximum amplitude is not much different from the eccentricity, which is displayed as a reference. The code therefore displays a highly magnified view of the “buckling.”

Quotes are used above because at these early times response is dominated by wave propagation. Low amplification and wave propagation to times near $\tau = 2$ can be seen from the amplification functions in Figure 2.3. Maximum amplification is about 2, and at these very early times the higher modes come into play. These have real wave velocities (oscillatory response) instead of imaginary wave velocities as in the lower, hyperbolic growth modes with $\eta < 1$. When you focus on this early motion you will see bending waves propagate out from the impacted end. Also, the wavelengths of motion are much shorter than for the later hyperbolic growth phase.

On the other hand, if you focus on very large times (not greater than 12 for practical application, as just discussed in the previous Section) the bar seems to just buckle into a fixed pattern that simply grows with time. The early bending wave propagation is still there, but you don't see it because it's too small on the screen, which has been automatically adjusted to display the highly amplified buckling at τ_{\max} .

These very small amplitude early-time waves were observed in the high magnification of optical lever arm measurements (Lindberg) but at the time were not understood in the absence of easily-generated computer movies. Attention was focused on later-time buckling, which was understood via less intensive calculations of the type in this book.

At this point you should view the movies to really get a feel for impact buckling motion and reveal for yourselves the many interesting features for various time frames. The code displays instructions prior to calculating and displaying the motion in time frames and increments you specify. These are repeated here for convenience:

Buckling of a Bar Under Eccentric Impact

²This code is distributed with the electronic version of this Little Book.

The amplitude of buckling relative to the initial eccentricity depends only on a dimensionless time τ , which is equal to the actual time times the axial impact strain times the bar wave speed divided by the radius of gyration of the bar cross section. In more physical terms, τ is the number of times a wave would traverse a radius of gyration, times the impact strain.

You are asked to enter an increment value for τ and then the number of increments for which buckling will be calculated. The program then calculates the buckle shape at each value of τ , after which the maximum buckle amplitude is displayed. Hitting any key then gives a graphical display of the bar about to hit a massive block at the left of the screen. The vertical line on this block represents the size of the initial eccentricity at the scale used to plot buckling for the τ range you specified.

(Hit any key for next screen)

Each time you hit a key at this point the buckle shape at the next time increment is displayed. If you hold a key down the display will show the buckling in movie action. The movie repeats over and over until you hit an "s" to stop and input new τ parameters, or "q" to quit the program.

Notice that at early times very small buckles propagate up the bar as they grow. At later times, when buckling grows very rapidly, the buckles remain nearly fixed in position. To see these aspects of buckling, chose various sizes and numbers of τ increments to span different τ ranges at various time resolutions.

Note: Enter τ values in the form "0.4", not simply ".4" which does not conform to standard input and would give a runtime error.

Hit any key to begin.

2.7 Dynamic Buckling With Random Imperfections

Another form of imperfection, more uniquely concerned with the dynamic problem, is suggested by experiments to be described later in which a large collection of rubber strips were buckled over a wide range of dynamic thrusts. It was found that the strips buckled into wavelengths that varied randomly at each thrust, with a mean and standard deviation both inversely proportional to the square root of the thrust as indicated by (2.57). These results are consistent with the assumption that random imperfections in the strips are amplified by the buckling motion. Thus the resulting buckled form, although still random, has statistics determined by the buckling amplification function given by (2.50) and in Figure 2.3.

Several methods of representing a random function have been described by Rice in the study of filtering electrical noise. In the electrical problem the function represents the variation of current with time, $I = I(t)$. In the buckling problem here, the random function represents the variation of lateral displacement with distance along the bar, $w = w(\xi)$. Thus there is a close analogy between the two problems, with electrical current being associated with mechanical displacement, and time in the electrical problem being associated with axial position in the mechanical problem.

In the electrical problem, a noise signal $I_0(t)$, having Fourier components $a_n(\omega_n)$, is fed into a filter having an attenuation characteristic $F(\omega_n)$. The output signal is $I(t)$, having

Fourier components $A_n(\omega_n) = F(\omega_n)a_n(\omega_n)$. In the mechanical problem, the “input” is the initial displacement $w_0(\xi)$, having Fourier components $a_n(\eta)$, and the “output” is the buckled form $w(\xi)$, having Fourier components $g_n(\eta) = G(\eta, \tau)a_n(\eta)$. Because the mechanical problem contains one added variable, time τ , the amplification characteristic also depends on time as indicated by $G_n(\tau)$ in (2.50), which is denoted here by $G(\eta, \tau)$. However, at each instant the analogy is quite close. The only difference is that in the electrical problem the process is *stationary*; that is the currents continue indefinitely in time and the statistics are taken to be independent of time.

In the buckling problem, the boundary conditions at the ends of the bar must be met, so the statistics depend also on the position ξ , the variable analogous to time. If the buckle wavelengths are very short compared with the length of the bar, however, one would expect that some distance from the end of the bar the effect of ξ diminishes and the assumption of stationary white noise would be acceptable. With this assumption the two problems are completely analogous and all the theory available from the electrical problem can be used here. In fact, the electrical problem is solved over a finite time interval just as for the finite length bar here and then the interval is allowed to become arbitrarily long. This is analogous to limiting attention to positions removed from the supports in the mechanical problem.

It is not necessary to assume that the random imperfections are stationary; this assumption merely makes the mathematics simpler. Before this is done, consider a random form of imperfection that does satisfy the boundary conditions of simple supports at $\xi = 0$ and $\xi = \ell$. These imperfections are given by

$$w_0(\xi) = \sum_{n=1}^N a_n \sin \eta \xi \quad (2.73)$$

in which N will be specified later. The coefficients a_n are random normal, having mean value zero and standard deviation $\sigma(\eta)$. The normal or Gaussian probability distribution is shown in Figure 2.8. If it is further assumed that σ is constant over all wave numbers of interest, then (2.73) is called (non stationary) *white noise*. For $w_0(\xi)$ to remain bounded, σ must ultimately die off for large η . Since our central concern is in the buckled shape $w(\xi)$ after the Fourier coefficients have been amplified by $G(\eta, \tau)$, and Figure 2.3 shows that for $\eta > 2$ the amplification is very small, harmonics with $\eta > 2$ can be safely neglected. Thus, in the initial deflections given by (2.73), we merely specify that $\sigma(\eta)$ dies off in some unspecified manner for $\eta > 2$ and is constant for $0 < \eta \leq 2$. This is the usual assumption justifying use of white noise as a filter input.

Since the concept of white noise can be applied only when associated with a process that passes a finite band of wave numbers, we must defer any examples of random functions until after the amplification function, with its inherent cutoff, has been applied to give the buckled shapes. This function, repeated from (2.50), is

$$G_n(\tau) = \frac{g_n(\tau)}{a_n} = \begin{cases} \frac{1}{1 - \eta^2} \left[\frac{\cosh p_n \tau}{\cos p_n \tau} - 1 \right] & \text{if } \eta \neq 1 \\ \tau^2/2 & \text{if } \eta = 1 \end{cases} \quad (2.74)$$

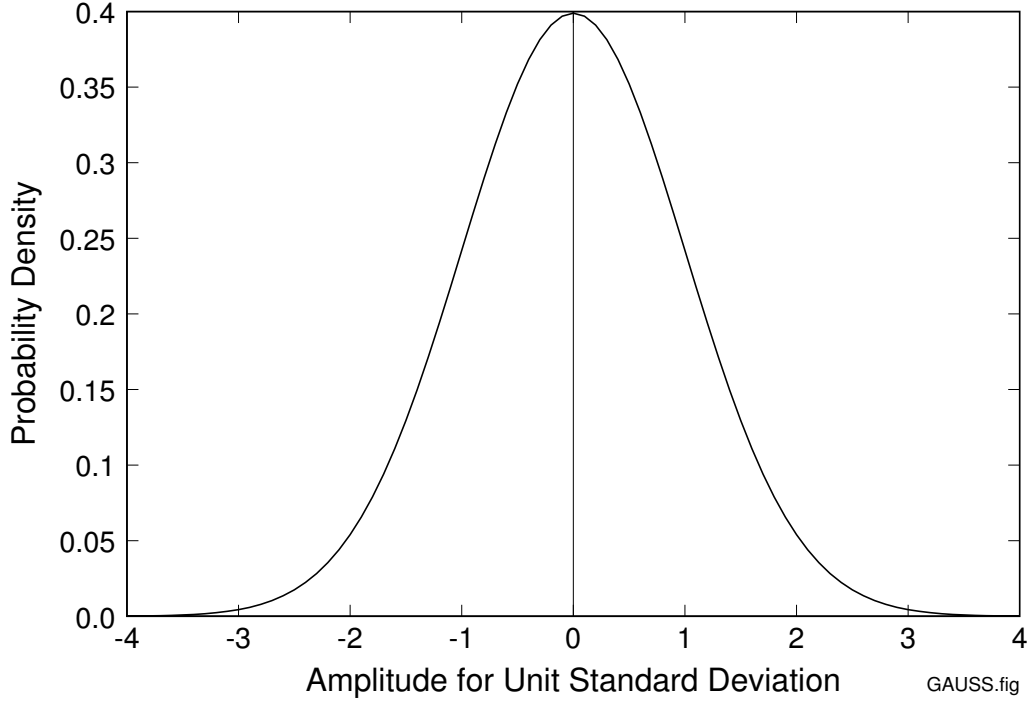


Figure 2.8: Assumed normal distribution of Fourier coefficients a_n of initial imperfections.

where

$$p_n = \eta |1 - \eta^2|^{1/2}$$

and the hyperbolic form is taken for $\eta < 1$. The buckled form is given by

$$w(\xi, \tau) = \sum_{n=1}^N a_n G(\eta, \tau) \sin \eta \xi \quad (2.75)$$

where N is the largest value of n for which $\eta \leq 2$.

With a cutoff function now applied, we can give examples of the shapes characteristic of buckling from random imperfections. Figure 2.9 gives two examples of buckled forms calculated from (2.75) using a length $\ell = 50\pi$, which is 25 complete Euler lengths and very long compared with the highly amplified wavelength $\lambda_p = 2\pi/0.8$ corresponding to $\eta = 0.8$. With this choice for ℓ the number of modes to be summed is $N = 100$ to span the interval $0 < \eta \leq 2$ of amplified modes. The procedure was to select 100 random numbers from a population having a normal distribution as in Figure 2.8, with standard deviation $\sigma = 1$. These were then used as coefficients a_n in (2.75) and the summation was taken over 100 modes. Higher harmonics would have had a negligible effect as already mentioned, because of the rapid decrease of $G(\eta, \tau)$ with η for $\eta > 2$.

In each of the two examples in Figure 2.9 (i.e., for each set of 100 random coefficients) the buckled shape is plotted at $\tau = 2, 4$ and 6 , with amplification functions as given in Figure 2.3. It is apparent in both examples that there are more crests (waves) at $\tau = 2$ than at $\tau = 4$, and more at $\tau = 4$ than at $\tau = 6$. This is because the peak of the amplification function is at higher wave numbers for the smaller times (Figure 2.3). Beyond about

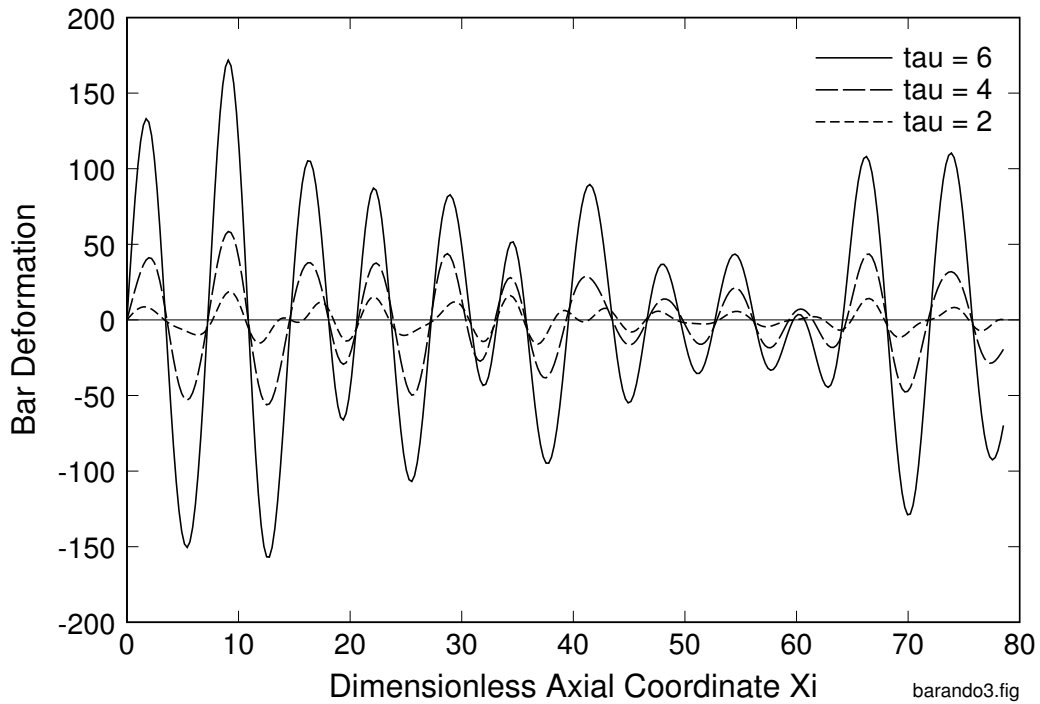
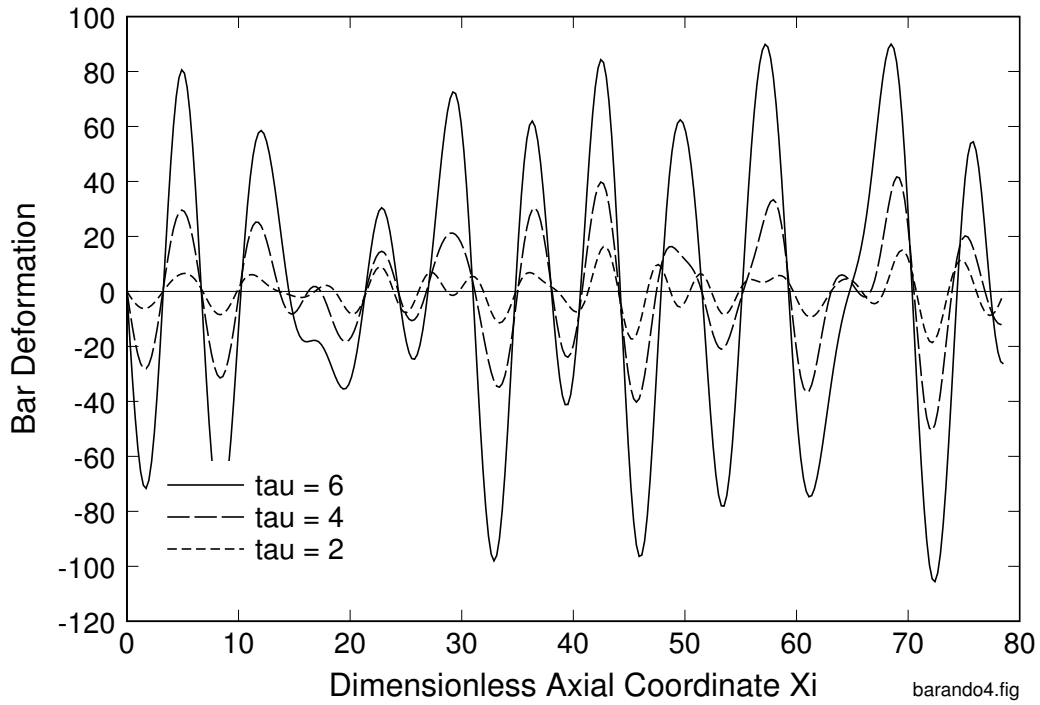


Figure 2.9: Two examples of growing buckles from random imperfections (100 modes, with a_n random normal with zero mean and unit standard deviation – separate set of a_n in each example; only half of total bar length $\ell = 50\pi = 157$ is shown).

$\tau = 6$ the number of waves tend to remain fixed because the shape of the amplification function becomes dominated by the hyperbolic modes, and the peak never shifts below $\eta = 1/\sqrt{2} \approx 0.707$. At this stage the waves remain nearly fixed in position and merely grow in amplitude.

Another feature exhibited in these examples is typical of buckled forms from white noise: although they consist of a random assemblage of harmonics, they exhibit a surprisingly regular pattern of waves. The average wavelength of this pattern depends, of course, on the region of amplification defined by the amplification function. In fact, an amplification function that is square in shape, constant for $\eta \leq 2$ and zero for $\eta > 2$, would give a wave pattern similar to those shown in Figure 2.9, but is *not* the waveform of the “actual” imperfection, whose Fourier components do not cut off at $\eta = 2$. This is the reason numerical examples had to be deferred to the discussion of buckled shapes; any specification of a cutoff wavenumber already implies *filtered* noise.

The only way to quantitatively describe buckle shapes as in Figure 2.9 for comparison with experiments is to calculate statistics of features of interest. One statistic can be calculated analytically: the expected (mean) value of the wavelengths. This can be done if we assume the buckling displacements are *stationary*, i.e., the bar is long enough that end conditions do not affect buckling some distance from the ends. With this assumption the initial imperfections can be represented by *stationary white noise* as follows:

$$w_0(\xi) = \sum_{n=1}^N a_n \sin(\eta\xi + \phi_n) \quad (2.76)$$

This form is similar to (2.73) except that here the Fourier components are added in random phase, with phase angles ϕ_n uniformly distributed (with equal probability) in the interval $0 \leq \phi_n \leq 2\pi$. The buckled displacements are then

$$w_0(\xi) = \sum_{n=1}^N a_n G(\eta, \tau) \sin(\eta\xi + \phi_n) \quad (2.77)$$

With the standard deviation of a_n constant, the theory in Rice can be used to determine that the mean wavelength between alternate zero crossings in the buckled form is

$$\lambda_m(\tau) = 2\pi \left[\frac{\int_0^\infty G^2(\eta, \tau) d\eta}{\int_0^\infty \eta^2 G^2(\eta, \tau) d\eta} \right]^{1/2} \quad (2.78)$$

Mean wavelengths from (2.78) were calculated numerically for τ ranging from 2 to 12. The results were only a few percent above the most amplified wavelength calculated with the approximate expression in (2.55). At $\tau = 8$ both formulas gave wavelengths very near the “preferred” wavelength $\lambda_p = 2\pi/0.8$ defined earlier. Thus, for practical application, mean wavelengths are essentially the same as most amplified wavelengths in this particular problem. We will see in Section 4 on cylindrical shells under axial load that the most amplified mode has $m = 0$ waves around the circumference, i.e., it is a symmetric mode. However, calculations with the two-dimensional counterpart to (2.78) show that the expected wavelengths are finite in both directions, so the probabilistic theory is essential to predict wavelengths in axial shell buckling.

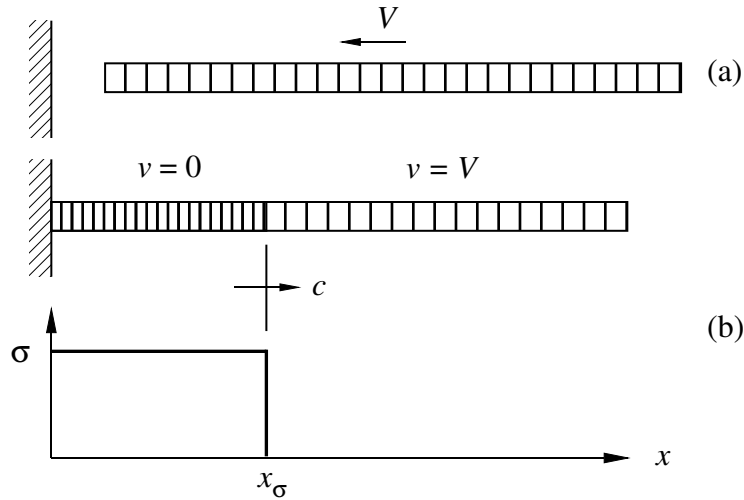


Figure 2.10: Axial stress wave in a bar impacting a rigid wall.

2.8 Experiments on Aluminum Strips

The essential results of the preceding theory of bar buckling from eccentric impact and with random initial imperfections were guided and confirmed by experiments on long bars impacted against massive anvils. To ensure that buckling took place with no twisting, and to minimize the size of testing machines needed, the experimental aluminum bars were thin strips about a half inch wide and 0.0125 inches thick. Accurate timing of the experiments and reproducible boundary conditions were obtained by producing the impact condition by first applying a tension and then suddenly cutting the strip some distance from the anvil, which was the lower jaw of a tensile machine. A compressive relief wave then traveled down the strip to the jaw, leaving the strip stress-free behind the wave and traveling at velocity $V = \sigma/\rho c$ toward the jaw.

This situation is pictured in sketch (a) in Figure 2.10, in which the strip is shown traveling toward a rigid anvil at velocity V . A gap is shown between the strip and anvil for clarity in imagining the process. At impact the left end of the strip comes to rest, and a compressive wave propagates away from the anvil at axial wave velocity $c = \sqrt{E/\rho}$. This wave brings an increasing length of bar to rest but now under compressive stress σ equal in magnitude to the initial tensile stress, sketch (b).

When the stress wave has passed a distance x_σ up the strip, the impulse applied by the end load at the rigid anvil must be equal to the initial momentum of the length x_σ brought to rest by the stress wave. This condition is expressed by

$$\sigma A \cdot \frac{x_\sigma}{c} = \rho A x_\sigma \cdot V$$

or

$$\sigma = \rho c V \quad (2.79)$$

This same reasoning can be applied to determine the velocity $V = \sigma/\rho c$ produced by the sudden release of the initial tensile stress.

An example of a strip buckled by this procedure was presented in Figure 1.2. The strip was made of aluminum alloy 6061-T6 with a 0.5 by 0.0125-inch cross section and a length of 30 inches between cutting notch and jaw. The photographs show only a few inches of the strip just above the jaw. The magnitude of the compressive wave was approximately 40,000 psi, about 15% below the yield stress. In the first three frames of the printed reproduction here the strip appears to be straight (18, 24 and 30 microseconds after stress arrival at the jaw), but in the original photographs slight bending can be seen at these early times. At 36 microseconds and 42 microseconds buckling is clearly visible near the jaw even in these poor reproductions.

Dimensionless times are given by (2.37) and (2.38)

$$\begin{aligned}\tau &= \frac{s^2 ct}{r} = \frac{\sigma}{E} \cdot \frac{ct\sqrt{12}}{h} = \frac{40,000}{10,000,000} \cdot \frac{200,000 \cdot \sqrt{12} t}{0.0125} \\ &= 222,000 t \quad t \text{ in seconds,} \quad = 0.222 t \quad t \text{ in microseconds}\end{aligned}$$

The times in Figure 1.2 are therefore expressed in terms of τ as follows:

t , microseconds	18	24	30	36	42	48	54	...	108
τ , dimensionless	4.00	5.33	6.67	8.00	9.33	10.7	12.0	...	24.0
Wave travel, inch	3.6	4.8	6.0	7.2	8.4	9.6	10.8	...	21.6

Thus, buckling was just perceptible in the original photographs at $\tau = 4$ and is just perceptible in the reproduction here at $\tau = 8$. Beyond $\tau = 12$ (54 microseconds) plastic hinges are forming and in the frames beyond 96 microseconds the upper waves are relaxing. The last row in the table is the distance the compressive wave has traveled up the bar after “impact” at $t = 0$. Even at the largest times in the figure the wave has traveled only about two thirds the distance up the 30-inch strip (21.6 inches at 108 microseconds), so the relaxing of buckles in these later frames is not caused by a relief wave from the free end of the strip. The relief is caused by the severe buckling near the impact end — the buckles allow the remainder of the strip to move downward without maintaining the impact stress. The wavelength of the lower buckle is about 0.47 inch, very close to the value 0.45 inch calculated as the preferred wavelength λ_p from the theory.

About 50 aluminum strips were buckled in this manner so that statistics of buckle wavelengths could be calculated. In these experiments lateral restraining blocks were placed a small distance on each side of the strips to suppress large-amplitude plastic hinges of the type in Figure 1.2. Several modestly plastic buckle waves were then observed in each strip by sighting down the shiny surfaces. These were initiated by elastic buckling, with the modest plastic response following in the same wavelengths. Results are presented as a histogram in Figure 2.11b.

For comparison, 65 buckle shapes from random imperfections were calculated as in Figure 2.9, each with a different set of 100 random values for a_n . Wavelengths in each buckled shape were then measured for $\tau = 6$ and the histogram in Figure 2.11a was prepared. Wavelengths were measured between alternate zero crossings for the first three waves from the support $\xi = 0$, not counting the support as a crossing. Separate histograms were also prepared for the first, second, and third waves individually. No

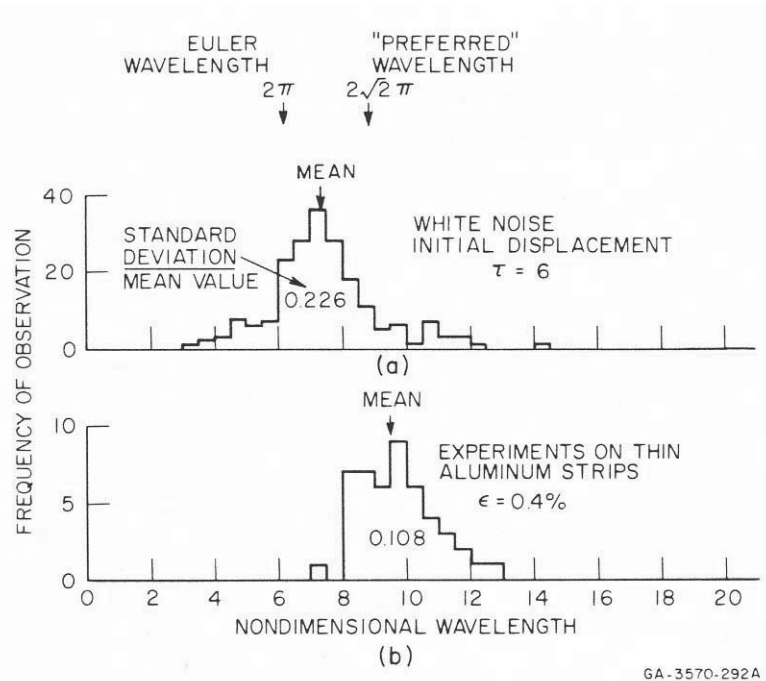


Figure 2.11: Theoretical and experimental histograms of buckled wavelengths in aluminum strips.

significant differences were found, indicating that the end support does not seriously affect wavelengths even a small distance from the support.

Many more computations would have to be added before this would approximate the probability distribution, but the main features of the distribution are apparent. The mean wavelength is $\lambda_m = 7.4$, not much different from the preferred wavelength $\lambda_p = 7.85$. The standard deviation is $\sigma_\lambda = 1.7$ and the ratio of standard deviation to mean wavelength is $\sigma_\lambda/\lambda_m = 0.23$.

The mean value of the buckle wavelengths in Figure 2.11b from the experiments is somewhat larger than in the theoretical histogram ($\lambda_m = 9.5$ compared with $\lambda_m = 7.4$), and the spread of wavelengths is somewhat smaller. The narrower spread possibly results because part of the initial imperfection in the experiments was in the form of impact eccentricity, which tends to produce a fixed wavelength as described in Section 2.5. However, the general features of the observed experimental distribution are adequately represented by the white noise theory. More extensive examples were obtained with experiments on rubber strips, which were less expensive and more extensive in the range of impact strains that could be produced.

The theory, of course, is not strictly applicable to the impact problem because it assumes that the thrust is uniform throughout the length of the bar. In impact, the thrust is applied by the moving axial stress wave, and at each instant only the distance enveloped by the wave is under compression. However, by the time significant buckling takes place the axial stress wave has traveled up the bar many wavelengths of the buckling that follows. For example, in Figure 1.2, the wave at 18 microseconds ($\tau = 4$) when buckles are barely visible has propagated 3.6 inches up the bar, which is more than 7 times the

full wavelength of buckling and 14 times the half wavelength at which buckling could commence. It is therefore highly unlikely that the moving stress wave has a significant effect on buckling.

This relationship between buckling onset and distance the axial stress wave has propagated up the bar can be stated more generally. From the theory we have seen that whether we assume the imperfections are local in nature, as in eccentric impact, or consist of a general random form over the bar length, the wavelength of the buckles is always close to the wavelength $\lambda_p = 2\pi/0.8$ of the preferred mode. Also, the magnification of buckling motion depends only on τ , all other essential parameters having been included in its definition. It seems reasonable to observe that effects of the axial stress wave motion will be small as long as significant magnification takes place only after the axial wave has passed several wavelengths along the bar. Without specifying a numerical value, we assume that the buckled form is unalterable determined (i.e., the buckled deformations are much larger than the initial imperfections) at a critical time

$$t_{cr} = \frac{r}{s^2 c} \cdot \tau_{cr} \quad (2.80)$$

Real time t can be expressed in terms of the number N of preferred wavelengths L_p through which the axial stress wave passes at velocity c :

$$t = \frac{L_p N}{c} = \frac{2\pi r}{0.8 c s} N \quad (2.81)$$

Substitution of this into expression (2.80) for critical time and use of the definition of s in (2.38) gives

$$N_{cr} = \frac{0.8 \tau_{cr}}{2\pi} \cdot \frac{1}{\sqrt{\epsilon}} \quad (2.82)$$

This suggests that the reasonableness of neglecting axial wave effects depends only on the compressive strain of the axial thrust. In metals this strain is very small within the elastic limit and, as we have observed, elastic buckling is adequately represented by the constant thrust theory. The yield strain in many engineering metals is about 0.004, so the minimum number of buckle wavelengths through which the axial stress wave passes before $\tau = 6$ is

$$N_{min} = \frac{(0.8)(6)}{2\pi} \cdot \frac{1}{\sqrt{0.004}} = 12.1 \quad (2.83)$$

This is 24 Euler lengths (half waves) before substantial buckling begins. The first half wave is traversed at $\tau = 6/24 = 0.25$, when the maximum amplification is still essentially zero (see Figure 2.4). Thus, the thrust is essentially uniform throughout each buckle wave, and even several waves, before any substantial buckling motion takes place. With the axial impact stress less than the yield stress in the elastic buckling under consideration, N_{cr} is larger than this minimum and even less buckle motion takes place during passage of the axial wave.

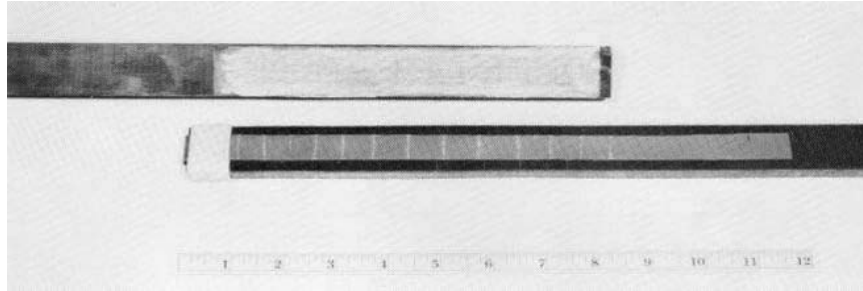


Figure 2.12: Apparatus and typical record for buckling rubber strips.

2.9 Experiments on Rubber Strips

Since (2.82) suggests that axial wave front effects, if any, would be more pronounced at large compressive strains, confidence in the theory would be enhanced for metals if it could be demonstrated experimentally that the theory is acceptable in a material that can withstand large elastic compressive strains. Pure gum rubber is such a material, and experiments have been performed using this material to strains up to about 15%.

The apparatus for these experiments, shown in Figure 2.12, is very simple and can be used for classroom demonstrations. A strip of pure gum rubber 0.0375 x 0.50 inch (0.95 x 12.7 mm) in section and about 1 foot (0.31 m) long was looped over one end of a rigid support bar and secured by means of masking tape as shown, with extra layers of tape wound above and below the rubber strip so that its end was separated from the support bar and the cover bar. The cover bar is shown above this assembly in the photograph. A strip of emery cloth has been glued to it and saturated with chalk dust.

In an experiment, the free end of the strip was held between thumb and forefinger, the cover bar placed over the strip, chalked side down and not touching the strip, and then the strip was stretched to a specified strain and released. The wrinkled strip impacted the chalk bar with sufficient velocity that a well-defined line was left on the strip at the crest of each wave, as shown. The positions of these lines were easily measured to an accuracy of 0.01 inch (0.25 mm).

To examine the applicability of the random noise assumption for imperfections, in addition to the applicability of the constant thrust theory, many experiments were performed so that statistical distributions could be prepared. Figure 2.13 gives histograms of the measured wavelengths for several values of initial tensile elongation. These data were taken from tests on 18 strips, each tested at all the strains, from smallest to largest strain in order to minimize any perturbations caused by the wrinkling of a previous test. Buckling at a strain greater than 25% is rather violent and leaves the strip with a definite bias toward the corresponding wavelength. The number of waves observed in each test varied from 2 to 3 at 3% strain up to 12 at 16% strain. The same strip tested repeatedly at the same strain gave an almost identical wave pattern each time, consistent with our mathematical model in which the imperfections are assumed random but fixed for any given bar. Data from only the first test at each strain were used for the histograms. Each histogram has a total of 65 observations so they can be compared directly.

It is significant that the general shape of all the histograms is the same and that the

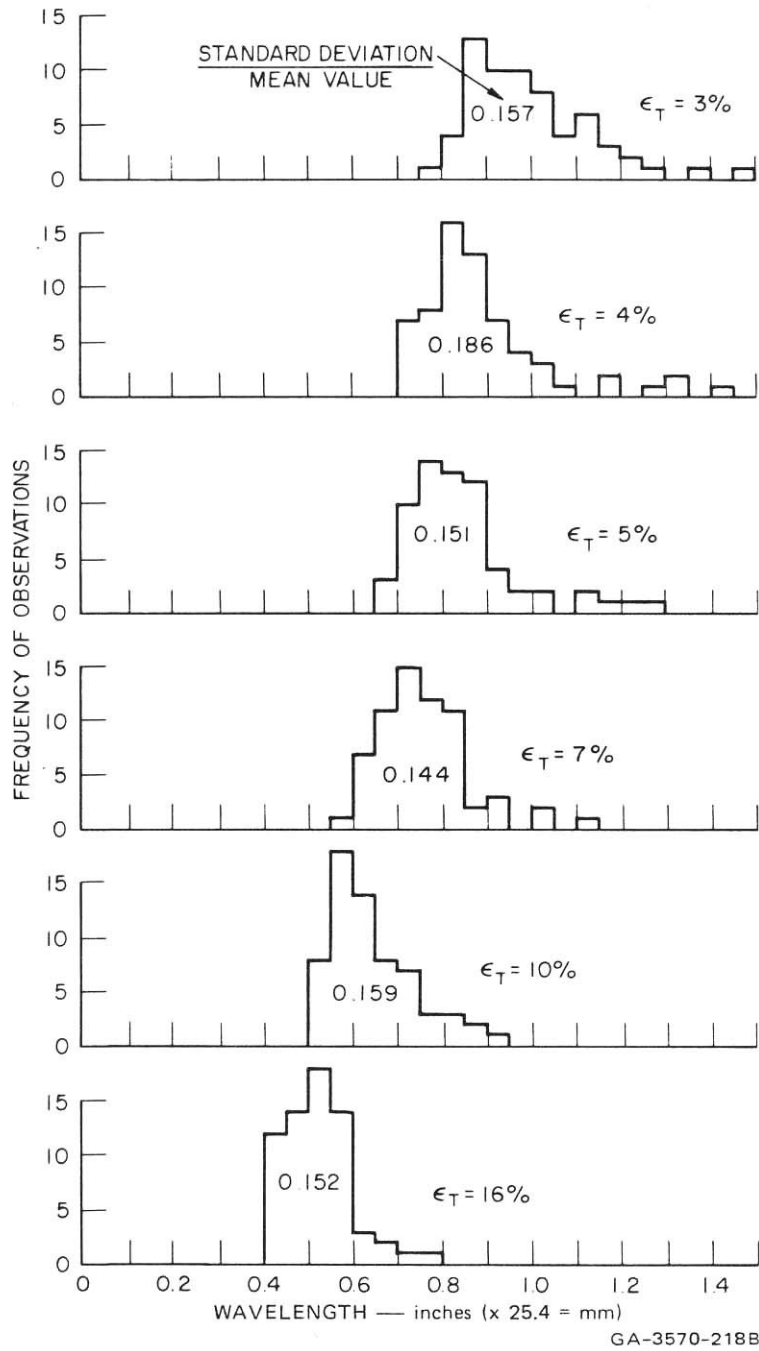


Figure 2.13: Histograms of observed buckle wavelengths for several initial tensile strains in gum rubber strips.

ratio between the standard deviation and mean value is nearly constant over the entire range of strains, as shown in Figure 2.13. This demonstrates that the statistics are inherent in the buckling process and are not the result of errors in measurement. It also indicates that the strips had no preferred wavelength characteristic of a manufacturing process. If these distributions are compared with the distribution in Figure 2.11, calculated assuming that initial imperfections can be represented by white noise, we see that the white noise assumption gives a very good description of the observed buckling.

To compare the observed wavelengths with the uniform thrust theory, we must take into account the large strains involved. Only the final compressive strain resulting from the initial tensile strain is needed, so the corrections can be obtained without reference to the details of large strain-wave propagation. It is sufficient to assume that the rubber behaves elastically so that the potential energy stored in compression equals the initial potential energy in tension. Tensile stress-strain tests performed on sample strips showed that true stress was linear with elongation out to at least 100% with a Young's modulus of 285 psi. Thus the initial tensile force F in the strip is given by

$$F = E\epsilon \cdot \frac{A_0}{1 + \epsilon} \quad (2.84)$$

where A_0 is the unstressed cross-sectional area of the strip and $\epsilon = (\ell - \ell_0)/\ell$ is the elongation. The initial stored energy at uniform tensile elongation ϵ_T is equal to the work done by the end force $F(z)$,

$$U_T = \int_0^{\ell - \ell_0} F(z) dz = EA_0 \ell_0 \int_0^{\epsilon_T} \frac{\epsilon d\epsilon}{1 + \epsilon} = EA_0 \ell_0 \log_e(1 + \epsilon_T) \quad (2.85)$$

where z is in the position of the moving end of the strip. Similarly, the compressive energy stored in the strip is

$$U_c = -EA_0 \ell_0 \log_e(1 - \epsilon_c) \quad (2.86)$$

expressed so that the compressive strain ϵ_c is a positive quantity. When these energies are equated, the compressive strain is found to be simply

$$\epsilon_c = \frac{\epsilon_T}{1 + \epsilon_T} \quad (2.87)$$

Further, the increased thickness h from the unstressed thickness h_0 , assuming to very high accuracy that the rubber is incompressible compared with these shear-dominated deformations, is

$$h = \frac{h_0}{(1 - \epsilon_c)^{1/2}} \quad (2.88)$$

The last correction to be made accounts for the wrinkles being formed at axial strain ϵ_c but measured when the strip has returned to zero strain. The ratio of the observed wavelength ℓ_r to the wavelength while under compression is, by the definition of ϵ_c ,

$$\frac{\ell_r}{\ell_c} = \frac{1}{1 - \epsilon_c} \quad (2.89)$$

The first approximation for the wavelength of the “most amplified” mode in dimensionless coordinate ξ is $\lambda_p = 2\sqrt{2}\pi$. Use of this with Equations (2.2.38) and $r = h/\sqrt{12}$ gives for the wavelength of the most amplified mode while the strip is under compression

$$\ell_{pc} = \pi \left(\frac{2}{3}\right)^{1/2} \frac{h}{\epsilon_c^{1/2}} \quad (2.90)$$

After the strip has relaxed, this preferred length would be elongated according to (2.89). Use of (2.90) in (2.89) with (2.87) and (2.88) gives for the elongated length

$$\ell_{pc} = \pi \left(\frac{2}{3}\right)^{1/2} \frac{(1 + \epsilon_T)^2}{\epsilon_T^{1/2}} h_0 \quad (2.91)$$

In Figure 2.14 the observed wavelengths of Figure 2.13 are plotted against this preferred length, the circled points giving the mean values and the bars extending one standard deviation above and below the circles. The mean values fall very close to a straight line through the origin, and the ends of the standard deviation bars are also closely bounded by straight lines. These observations suggest that (2.91) gives the proper form of variation with strain. However, the ratio between observed and preferred wavelengths (the slope of the line through the circles) is 1.70 here as compared with only 1.07 for the aluminum experiments given in Figure 2.11. This difference is attributed to strain-rate effects in the rubber. If, for example, these effects are lumped into an effective dynamic compressive modulus k times the static tensile modulus, the preceding theory gives a slope of 1.00 for $k = 2$.

Although the foregoing interpretation of the discrepancy between the aluminum and rubber experiments is somewhat speculative, the smooth variation of measured wavelength with strain strongly supports the conclusion that the moving axial-stress front has a negligible effect on the wrinkle formation and that a constant-thrust theory can be used with confidence. The main effect of the traveling thrust is that the duration of the thrust decreases as one moves away from the struck end, and this could easily be accounted for by simply assigning a different duration to each wrinkle. This conclusion should also be applicable to more complicated structures, such as cylindrical shells under axial impact. For large deflections, it might also prove necessary to compute a new thrust for each wave, reduced owing to lateral deflections in preceding waves.

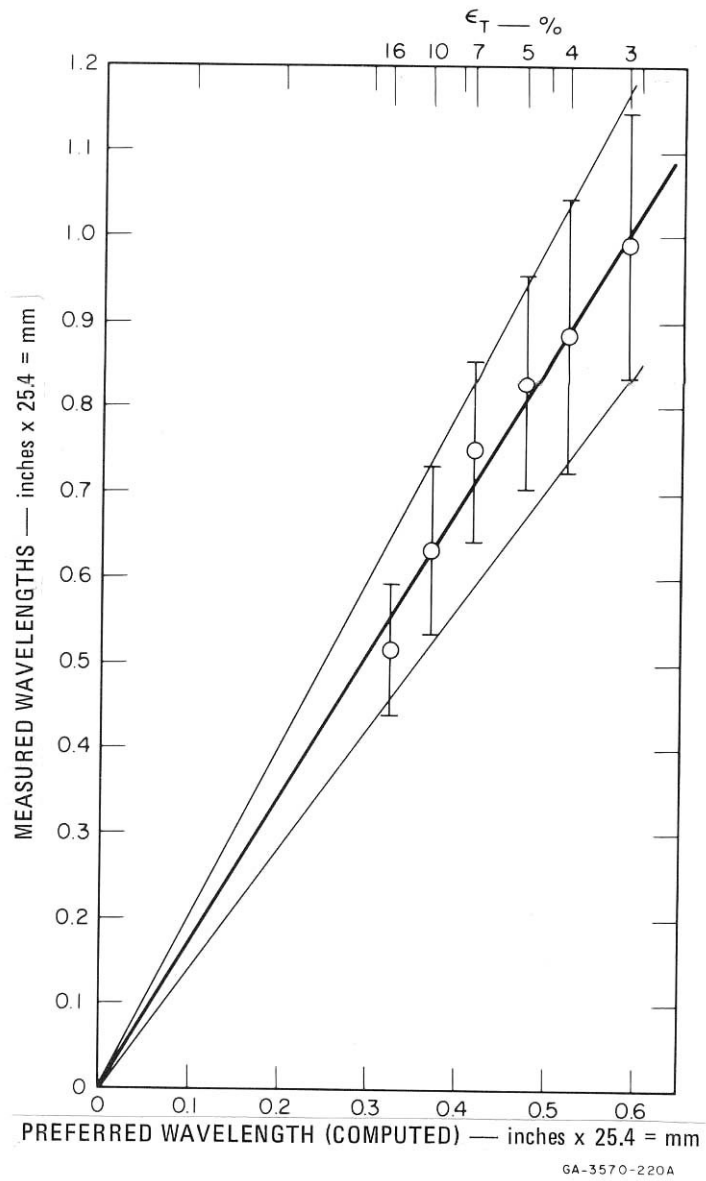


Figure 2.14: Measured wavelength versus calculated wavelengths (bars extend one standard deviation above and below the mean values).